Effect of Cell Geometry and Gap Junction Conductance on Wave Propagation in Myocardium: A Computational Approach

By:

Amadou Toure

A dissertation submitted to the Graduate Faculty in Engineering in partial fulfillment of the requirements for the degree of Doctor of Philosophy, The City University of New York

2011

This manuscript has been read and accepted for the
Graduate Faculty in Engineering in satisfaction of the
dissertation requirement for the degree of Doctor of Philosophy.

Date

Prof. Barry Gross, Dept. of Electrical Engineering
Chair of Examining Committee

Date

Prof. Mumtaz Kassir
Executive Officer

Prof. Candido Cabo, Dept. of Computer Systems, New York City Tech

Prof. Lucas C.Parra, Dept. of Biomedical Engineering

Prof. Maron Bikson, Dept. of Biomedical Engineering

Prof. Susannah Fritton, Dept. of Biomedical Engineering
Supervisor Committee

THE CITY UNIVERSITY OF NEW YORK

Abstract

Effect of Cell Geometry and Gap Junction Conductance on Wave Propagation in Myocardium: A Computational Approach

by

Amadou Toure

Adviser: Professor Candido Cabo

The conduction velocity and the path of propagation of electrical waves determine the effectiveness of contraction of the heart muscle. Areas of slow conduction and block may lead to the formation of cardiac arrhythmias, which may result in cardiac fibrillation and sudden cardiac death. Propagation of cardiac waves is determined by both passive and active properties of myocardium.

Cardiac disease, like heart failure and myocardial infarction, as well as aging result in changes in cell geometry and the remodeling of the ionic channels and intercellular gap junctions. The main objective of this thesis is to determine the effect of the cellular microstructure like cell geometry and intercellular gap junctions on propagation of the cardiac waves, using a sub-cellular computer model of myocardium.

We found that variations in cell size, with a constant cell length/width ratio, shows small effects on conduction velocities. The results were not dependent on gap junction distribution and conductance, or the details of the tissue architecture. Other parameters kept constant, length/width was a good predictor of the velocity of propagation and anisotropic ratio. These results indicate that cell shape is more important than cell size in determining conduction velocity of the propagating wave.

We also found that structural heterogeneities, due to spatial hetorogenetities in cell geometry or gap junction conductance lead to conduction block (a precursor of cardiac arrhythmias). Both, cell geometry and gap junctional conductance (among other factors) determine the tissue space constant. Conduction block occurred when a wave propagated into regions with a larger space constant ($\sim 40 - 50\%$ increase). As the ratio cell length/width increases the tissue space constant is less sensitive to changes in cell geometry and gap junction conductance. As a consequence, tissue

architectures with more elongated cells (i.e. higher length/width ratio) are less sensitive to structural heterogeneities resulting from cell geometry and gap junction conductance. This findings may have important implications for tissue engineering, and the design of cardiac tissues.

Acknowledgements

I am so ever grateful to the Creator of this universe in allowing me to accomplish this work.

Table of Contents

List of Figures

Chapter 1

Introduction

Over 600,000 people die of heart disease per year in the U.S.A. Most of those deaths are the result of cardiac arrhythmias including ventricular fibrillation [132].

A substantial research effort has been devoted to the understanding of the mechanisms of cardiac arrhythmias. Conditions that lead to slow propagation of the cardiac impulse and conduction block are known factors that favor the development of arrhythmias [64].

While most of the current understanding of the mechanisms of arrhythmias comes from experimental studies, computer simulations have provided important insights into the mechanism of propagation and block [64].

Computer modeling and simulation has been shown to be an important tool for interpreting and integrating different experimental data at a different scale in cardiac electrophysiology as well as for producing testable hypothesis. Computer modeling of excitable tissues, based on the pioneering work of Hodgkin and Huxley [52], has grown in complexity as more experimental data at the tissue, cellular and molecular level becomes available. Todays models incorporate the biochemistry, biophysics and geometry of cells, and anatomy of tissues and organs [55]. The task, however, is not trivial. Such computer simulations require a wide range of numerical techniques, spatial and temporal scales to accommodate the various levels of integration (molecule, protein, cell, tissue, organ, and organ system).

1.0.1 Motivation

Propagation of the cardiac impulse is dependent on the active electrical properties of the myocyte membrane, eg. ionic current flow through ionic channels and ionic concentration, as well as the passive properties of the cellular network, eg. cell geometry, surface to volume ratio, intracellular and extracellular resistances, and intercellular proteins. Some of the effect of these passive properties of cardiac tissue on the propagation of the cardiac impulse have been demonstrated experimentally and in continuous computer models of propagation.

Theoretical and experimental studies have shown that cell geometry plays a role in determining conduction velocity [56]. In a single fiber, conduction velocity is approximately proportional to the square root of the fiber radius [56]. It is also well established that in multi-dimensional myocardium, conduction velocity of flat waves decreases with an increase in cell membrane surface/volume ratio [56]. Cardiomyocyte geometry varies among species [106], and for the same specie, it changes with development [112, 118]. Cell geometry could also be affected by disease [128]. Experimentally, cell size is usually estimated from measurements of cell length and cell width [118, 128]. A number of reports point to the importance of cell size on cardiac electrophysiology [112, 118, 128]. However, the mechanism of the effect of cell size on conduction velocity and wave propagation remains unclear.

Intercellular proteins are also major determinants of propagation [54, 19]. Intercellular proteins are affected by disease (myocardial infarction), and the reduction in intercellular proteins and gap junction conductance results in a reduction of the conduction velocity of the propagating wave [101, 99]. Several researchers have studied the effect of gap junction distribution and gap junction remodeling on propagation in cardiac tissue [112, 118, 20, 117].

Our objective is to determine the effect of the microstructure like cell geometry and gap junctional conductance, as well as spatial heterogeneities of those parameters on wave propagation in myocardium. To achieve our objective we implemented a sub-cellular computer model of myocardium.

1.0.2 Organization of this Thesis

In Chapter 2, we present a brief review of cardiac physiology. We begin with the crucial role of the hearts pumping mechanism and its dependence on its electrical excitation. We then explain in detail the cellular components responsible for the excitation of the myocyte and its propagation from cell to cell throughout the heart.

In Chapter 3, we present the theory behind cardiac electrophysiological modeling; We illustrate the model of the single myocyte and trace its historical development. We then expand those concepts to modeling of propagation of the cardiac action potential in multicellular myocardium. Finally, we present the numerical techniques used to implement these models.

Following these two introductory chapters, we then address the main topic of this thesis. Chapter 4 presents the effects of cell geometry on conduction velocity. In chapter 5, we present the effects of structural hererogeneities in cell geometry and gap junction conductance on conduction block. Finally in Chapter 6 we discuss the implications of our findings, in cardiac electrophysiology and tissue engineering, and discuss possible experiments that could be designed to test experimentally our theoretical findings as well as future studies.

Chapter 2

Cardiac Physiology

The main function of the heart is to pump blood such that oxygen and nutrients can reach all cells in the body. The pumping mechanism of the heart results from the synchronous contraction of its different chambers: atria and ventricles. Cell contraction follows the electrical activation of the cell by the action potential (AP). With each AP comes an increase in free cytosolic concentration of calcium, which through the contractile machinery [9], gives rise to myocardial contraction. The pattern of propagation of the action potential in the heart, which is initiated in the sino-atrial node, a group of specialized cells located on the wall of the right atrium and followed with the activation of the atria and the ventricles (see below), is designed to produce a synchronous and forceful contraction of the heart.

2.1 Basic Anatomy and Blood Flow

Figure 2.1 illustrates the interior of the mammalian heart with its four chambers: right and left atria and right and left ventricles. Valves (atrioventricular valves) between the atria and ventricles maintain a unidirectional flow of blood from the atria to the ventricles; the atria are receiving chambers of the heart, and the ventricles are the distributing chambers.

Oxygen-poor blood from the body organs returns to the heart's right atrium via the major veins

(superior and inferior vena cava). The blood in the right atrium passes into the right ventricle through the tricuspid valve, and from there is ejected to the pulmonary artery on the way to the lungs, where oxygen uptake follows, (see figure 2.1).

Oxygen-rich blood returning from the lungs enters the left atrium via the pulmonary veins. This oxygenated blood passes into the left ventricle through the mitral valve, where it is ejected to the aorta to supply the systemic circulation (the rest of the body) except the lungs, (see figure 2.1).

Blood supply to the heart itself is achieved by the left and right coronary arteries, which branch off from the aorta. The right coronary artery supplies principally the right ventricle and atrium; the left coronary artery, divides near its origin into the anterior descending and circumflex branches, supplies principally the left ventricle and atrium [10],(see figure 2.2). Any failure in the coronary blood flow impairs oxygen delivery to the myocardium. This will result in impairment in the electrical and mechanical function of affected myocardium, causing irregularity of heart rhythm (cardiac arrhythmias), and possibly necrosis (cell death) for severe and prolonged reduction of coronary flow.

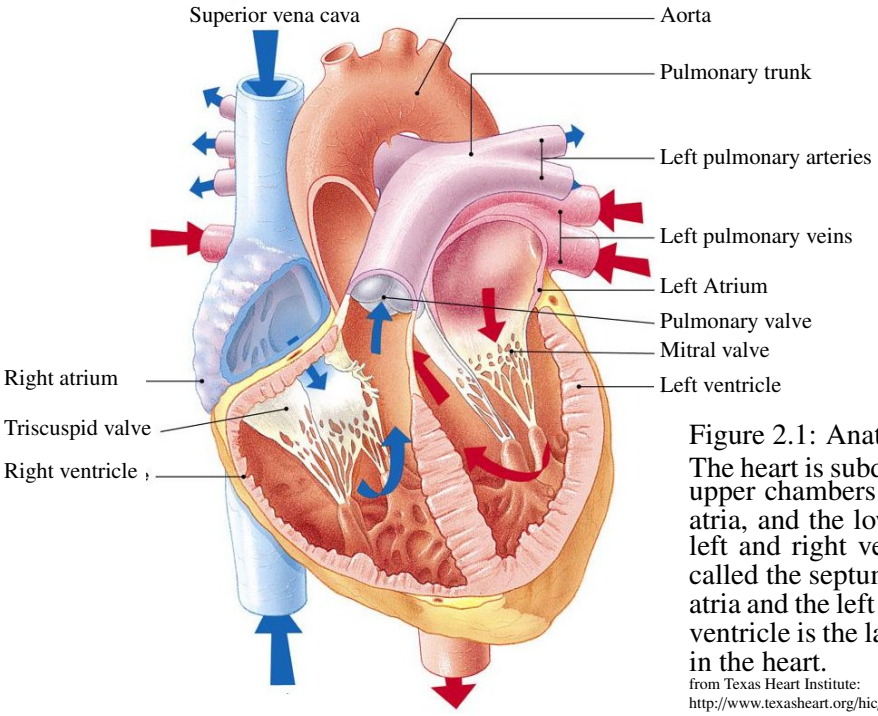

Figure 2.1: Anatomy of the Human Heart
The heart is subdivided into 4 chambers. The upper chambers are called the left and right atria, and the lower chambers are called the left and right ventricles. A wall of muscle called the septum separates the left and right atria and the left and right ventricles. The left ventricle is the largest and strongest chamber in the heart.
from Texas Heart Institute:
http://www.texasheart.org/hic/anatomy/anatomy2.cfm

The ventricles are the primary power generator for blood pumping. The atria are more like

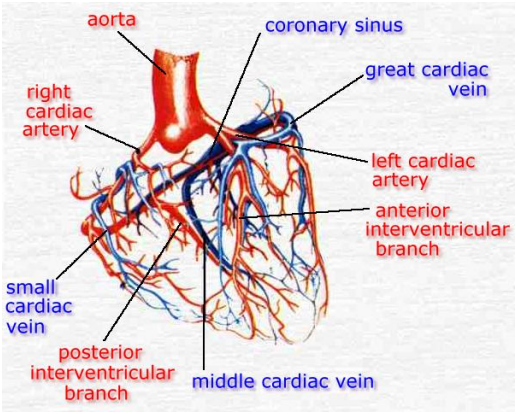

Figure 2.2: Distribution of the coronary arteries and veins
The left and right coronary arteries and their branches lie on the surface of the heart, and therefore are sometimes referred to as the epicardial coronary vessels. These vessels distribute blood flow to different regions of the heart muscle.
from http://www.cvphysiology.com/Blood%20Flow/BF001.htm

reservoir conduits for their respective ventricles [10]. The left ventricle has to overcome a greater vascular pressure in order to pump blood around the entire body. As opposed to the right ventricle that needs only pump blood to the lungs. The right ventricle requires only one seventh of the mean pressure developed by the left ventricle. Therefore the left ventricle is the biggest and thickest chamber of all [10].

2.2 Microscopic and Cellular Structure

2.2.1 The Myocardium

The atria and ventricles are blood filled cavities surrounded by walls. The walls are primarily a muscle structure, the myocardium (heart muscle). The myocardium is covered inside and outside by layers of flattened epithelial cells and connective tissue, the endocardium and epicardium respectively, (see figure 2.3). On the endocardial side of the ventricles, the Purkinje system provides a fast conduction pathway to produce a synchronous activation of the ventricles. To perform its function as the major blood pumping chamber, ventricular myocardium is much thicker than the atrial, with the myocardium of the left ventricle being the thickest structure of the heart. In humans, the right ventricle is $5mm$ thick vs $20mm$ for the left ventricles, whereas the atria is $2-3mm$ thick [44]. The myocardium is composed of several cell types that include smooth muscle cells, fibroblasts, and cardiac myocytes. The fundamental contractile cell of the myocardium is the myocyte.

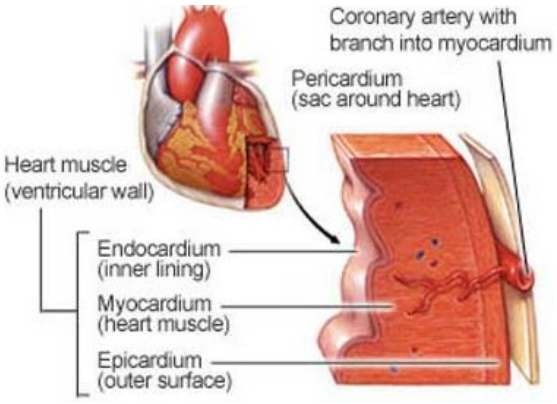

Figure 2.3: layers of the heart.
The myocardium is covered inside and outside by layers of flattened epithelial cells and connective tissue, the endocardium and epicardium respectively.
from http://www.ohiohealth.com/mayo/images/image_popup/r7_heartmuscle.jpg

2.2.2 The Myocytes

From a microscopic view, myocardium consists primarily of discrete myocytes (cardiac cells). In the heart, there are myocytes with specialized functions (pacemaking, conduction, or working). Pacemaking myocytes, located in the sinoatrial node have the task of initiating the heart beat by automatically initiating the electrical excitation (action potential) of the pacemaker region (the sinoatrial node). The action potential then propagates and activates atrial cells. After the atria are activated, the propagating wave proceeds through the atrioventricular conducting system, to activate the working cells in the ventricles.

Pacemaking cells in the sinoatrial node have irregular spider or spindle shapes [104]. In humans, spider shaped myocytes have an extension of $92 - 102\mu m$ with a central body diameter of $7 - 9\mu m$, whereas spindles shaped cells have an extension of $115 - 130\mu m$ with a central body diagram of $5 - 7\mu m$.

Working cells of the ventricles and atrium are responsible for the contractile activity of the heart muscle. Since cells are electrically connected through gap junctions, propagation of the action potentials propagates from cell to cell. Myocytes of the mammalian working myocardium are of irregular cylinder shape with frequent branching processes (see figure 2.4) [10]. Working myocytes range from 50 to $120\mu m$ in length with a diameter between $5 - 15\mu m$.

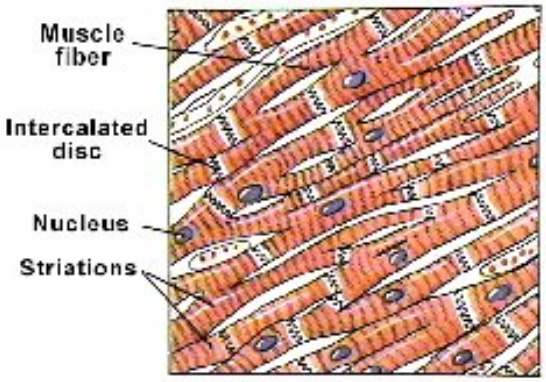

Figure 2.4: Structure of cardiac myocytes.
The myocytes, with branching geometry, are joined by intercalated discs to form a functional syncytium.

2.2.3 The Sarcolemma and its Ionic Channels, pumps, and exchangers

The sarcolemma is a semi-permeable thin barrier of phospholipid bilayer (membrane), $3-5nm$ of thickness that encloses the cardiac myocyte and separates the extracellular space from the intracellular space. The bilayer contains peripheral proteins attached to the surface and transmembrane proteins spanning over the sarcolemma, (see figure 2.5). These proteins are partly floating in the bilayer, but can also be fixed to elements of the cytoskeleton. Transmembrane proteins move ionis between the intracellular and the extracellular space by different mechanisms. Ion channels passively conduct ions down their electrochemical gradients through selective pores; pumps and transporters actively transport ions against their electrochemical gradient; exchangers electrogenically exchange ionic species. They have narrow, highly selective pores that selectively allow passage of specific inorganic ions, mainly Na^+, K^+, Ca^{2+},or Cl^-. The dynamic behavior of all those transmembrane proteins results in the action potential.

Ion channels have different functional domains [79]: an aqueous pore which is the pathway for ions to permeate, a selectivity filter permitting only certain ions to enter, a gate that regulates the permeation. The gating mechanism is regulated by specific stimulus: changes in the voltage across the membrane (voltage-gated channels), a mechanical stress (mechanically gated channels), or a binding of a ligand (ligand gated channels). Ligand gated channel can be either an extracellular mediator-specifically, a neurotransmitter (transmitter-gated channels)-or an intracellular mediator, such as an ion (ion-gated channels).

Channels are not coupled to an energy source to carry out active transport; the transport they mediate is always passive. The movement is driven by the potential energy of the ion concentration and voltage gradients [79]. The direction and magnitude of electrical current flow through an open ion channel depends on the concentration of permeable ion on either side of the membrane and the voltage across it. Ions tends to move down their concentration gradient (from high to low concentration "downhill").

2.2.4 Myocytes' Contractile apparatus

Cardiac muscle cells are made up of sarcomeres that contain thick filaments composed of myosin and thin filaments containing actin; (see figure 2.5). Chemical interaction between actin and myosin filaments during the process of excitation-contraction coupling causes the sarcomere to shorten as the myosin and actin filaments slide past each other, thereby causing the muscle cell to contract.

Calcium (Ca^{++}) modulates cardiac excitation-contraction coupling. The sarcolemma membrane of the myocyte surrounds the bundle of myofibril and has deep invagination called transverse (T) tubules(Figure 2.5). The T tubules, being a part of the external sarcolemma, are open to the external environment of the cell. This permits ionic exchanges between extracellular and intracellular compartments to occur deep within the myocyte during electrical activation of the myocyte. Within the cell, and in close association with the T tubules, is an extensive, branching tubular network called the sarcoplasmic reticulum (SR). Terminal cisternae are end pouches of the sarcoplasmic reticulum that are adjacent to the T tubules. Between the terminal cisternae and the T tubules are electron-dense regions called feet that are believed to sense calcium between the T tubules and the terminal cisternae. Closely associated with the sarcoplasmic reticulum are large numbers of mitochondria, which provide the energy necessary for myocyte contraction [63].

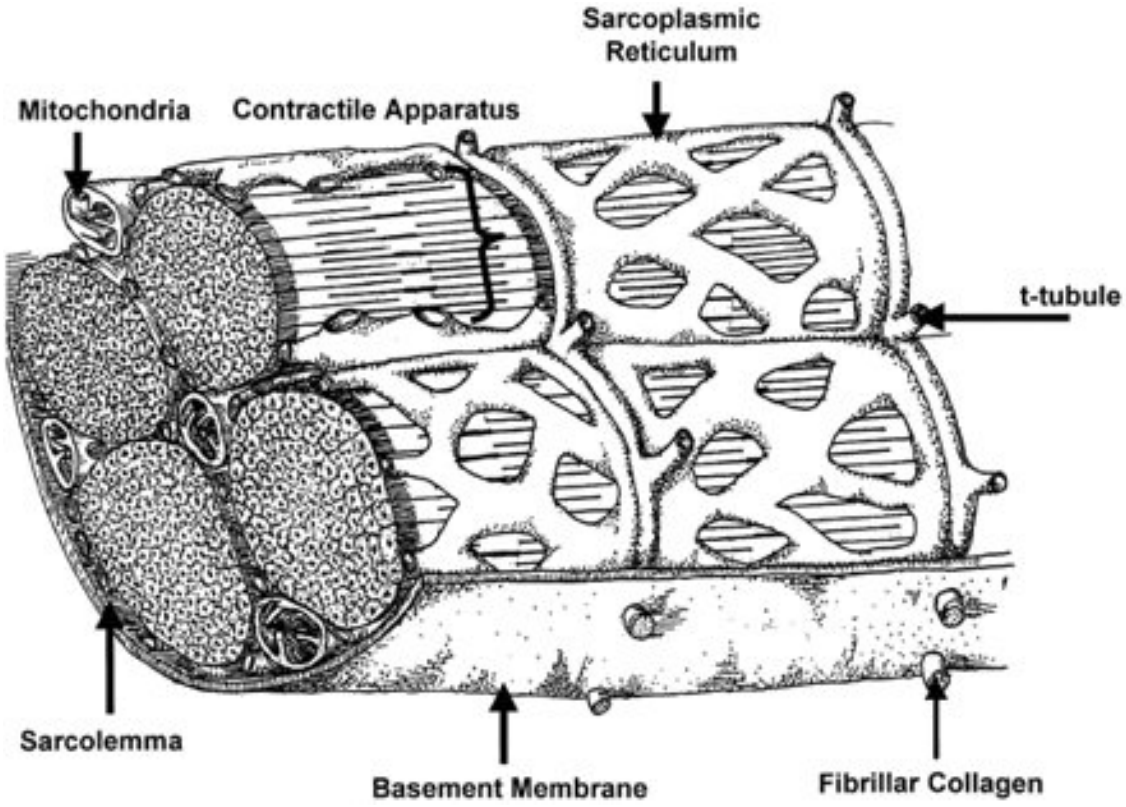

Figure 2.5: Longitudinal cross section of an individual cardiac myocyte. The sarcolemma, which enfolds the myocyte, contains integrins that bind the myocyte to the extracellular matrix, and also contains integral proteins that contribute to the action potential. Invaginations of the sarcolemma, which contains a high density of L-type Ca2+ channels, are the T tubules. This specialized region of the sarcolemma allows for the close apposition of the L-type Ca2+ channel to the Ca2+ release channels of the sarcoplasmic reticulum. The sarcoplasmic reticulum serves both as a source and an internal store of cytosolic Ca2+ required for excitation-contraction coupling. The contractile apparatus is a highly organized array of myofilament proteins composed primarily of thick myosin and thin actin filaments. The overlapping of these proteins form the dark and light bands as shown in this illustration. Cut in cross section are shown the numerous mitochondria, which are in close proximity to the myofilament apparatus.

2.2.5 Cardiac Muscle: a Functional Syncytium

In biology, a syncytium is usually defined as a large mass of cytoplasm containing many nuclei and enclosed in a cell membrane. The myocardium is not a true anatomical syncytium, because laterally the myocardial fibers are separated from adjacent fibers by their respective sarcolemma, and the end of each fiber is separated from its neighbor by dense structures, intercalated disks, that are continuous with the sarcolemma, (see figure 2.4). However, because myocytes are electrically well-coupled, cardiac muscle can be considered a functional syncytium. As a wave of excitation approaches the end of a cardiac cell, electrical excitation spreads to the next cell through high conductance channels between cells called gap junctions (nexi) [10].

2.2.6 Intercellular Ion Channels; Gap Junctions

Gap junctions are specialized membrane structures composed of multiple intercellular ion channels that facilitate electrical and chemical communication among cells [119].

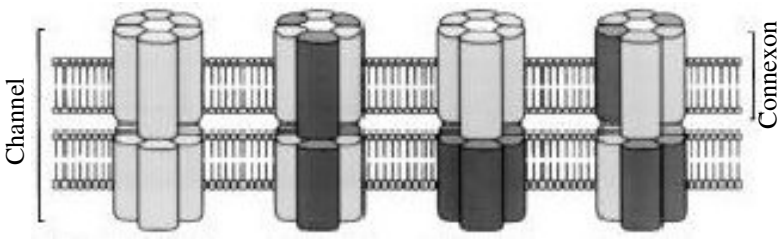

Figure 2.6: Nomemclature for connexons and gap junction formed by one or more connexins. Connexons composed of a single connexin are termed homomeric; those composed of a different connexin in each hemi-channel are heterotypic, and those with more than one connexin isoform in the hemi-channel are heteromeric
Modified from [61]

They are cylinder or barrel shaped with a diameter of $1.5 - 2.0um$ [34] and a length of approximately $2 - 12nm$. They couple the intracellular space of adjacent myocytes, and are located at the intercalated disk. A gap junction is build by two hemi-channels, so called connexons, piercing the sarcolemma of the involved cells, (see Figure 2.6). Connexons are formed by six integral membrane proteins, connexins. Connexins are named by their atomic weight ranging from 25 to $50KDa$ [34]. Three different connexins are prominently expressed in the mammalian heart: connexin-40(Cx-40), connexin-43(Cx-43), and connexin-45(Cx-45) [119]. The diversity of gap junction channels may

be amplified by the existence of channels composed of different connexins (see figure 2.6) [34]. Gap junction channels are permeable to ions and small molecules with molecular weights up to approximately $1kDa$ [119]. The connexin composition of a gap junction channel determines its ion selectivity, conductance, voltage sensitivity, and regulation. Ventricular muscle expresses predominantly Cx-43 and Cx-45, whereas atrial muscle and Purkinje fibers express all three cardiac connexins [119].

The directional dependence of intracellular electrical conduction, i.e. anisotropy, is due to a difference in density and length of gap junctions in both the longitudinal and transverse fiber direction. A longitudinal gap junction is oriented in the direction of the first principal axis of adjacent myocytes, whereas a transverse gap junction is oriented perpendicular to the principal axis. A propagating wavefront encounters a greater number of gap junctions per unit length in the transverse compared to the longitudinal direction, producing slower transverse than longitudinal conduction in normal myocardium(i.e., anisotropic conduction) [10].

2.3 The Electrophysiology of the Heart: The Action Potential(AP)

Since cardiac excitation is the precursor of the mechanical contraction of the heart, a substantial amount of research has been devoted to the understanding of normal and abnormal cardiac excitation and the propagation of the cardiac impulse. Similar to other reaction-diffusion processes, cardiac excitation involves a locally regenerative process (generation of the action potential by individual myocytes) with the transmission of this process through the flow of electric charge (conduction of the AP from cell-to-cell through intercellular gap junction). In addition, extracellular potentials resulting from the electrical activity of cells or from an external current ow can modulate the propagation and initiation of excitation.

Electrical stimuli applied to a myocyte at resting potential, triggers a sequence of actions involving the influx and efflux of multiple cations and anions through ion channels that together cause the transmembrane voltage to change rapidly from negative to positive and back. The change in

transmembrane voltage is the action potential.

Ion channels, pumps, and exchangers located in the myocyte membrane tightly regulate the movements of charges in and out of the cell. Therefore, they are the basis for the generation of the cardiac AP. Positive currents flowing into the cell, Na^+ and Ca^{2+} inward currents, depolarize the cell membrane (that is cause the transmembrane potential of the cell to be less negative), whereas positive ions flowing out of the cell, K^+ outward currents, repolarize the cell membrane (that is cause the transmembrane potential to be more negative). Since all these currents are flowing at the same time, the net current shifts will determine the actual changes in membrane potential.

2.3.1 Sequence of electrical excitation

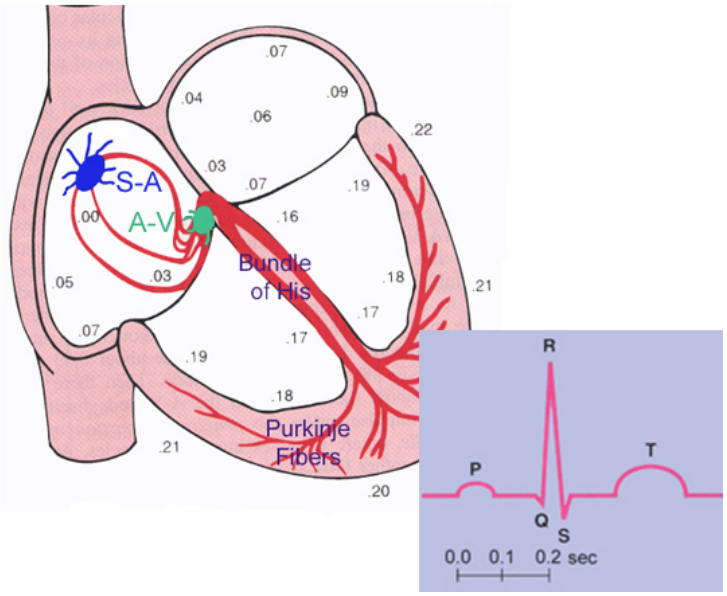

Figure 2.7: The cardiac conduction system showing time delays of impulse spread through the different parts.

Figure 2.7 shows the normal activation of the heart and the times at which an impulse initiated by the sinus node (SA node) reach different parts of the heart. Once the impulse is initated in the sinus node, the impulse spreads through the right atrium along ordinary atrial myocardial fibers before the left atrium is excited. A special pathway, the Backmanns bundle conducts the impulse from the SA directly to the left atrium. Conduction velocity in the atrium is about $1m/s$ and the activation of the atrium takes about $80ms$ [10]. The atriventricular (AV) node and Bundle

of His constitute the only pathway for conduction from atria to ventricles as these chambers are separated by a layer of fibrous non-conductive tissue. The AV node imposes a conduction delay a few tenths of seconds between atrial and ventricular excitation. This delay allows the filling of the ventricles by atrial blood. Once it crosses the AV node, the impulse spreads through the Bundle of His, with a fast conduction over the Purkinje fiber ($14m/s$). This fast conduction allows a rapid and coordinated activation of the entire endocardial surface of the ventricles necessary to create a forceful ventricular contraction [10].

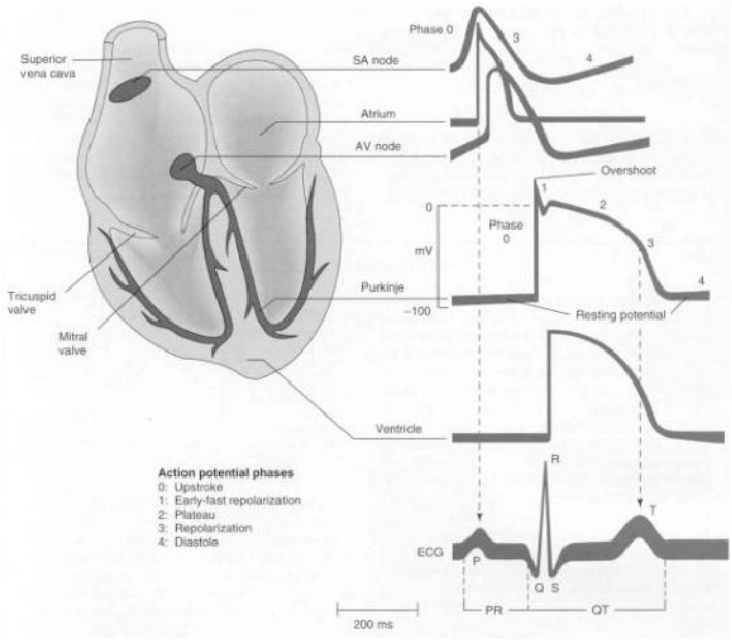

Figure 2.8: Interrelation between cardiac action potentials and the electrocardiogram

2.3.2 Different Types of Cardiac Action Potential

Figure 2.8 shows the action potentials characteristic of the different regions of the heart. Action potentials recorded in the contracting regions (atria and ventricle), as well as in the specialized conducting fibers(Purkinje fibers) show a fast depolarizing action potential. The action potentials found in the pacemaking sinoatrial (SA) node, and in the conducting atrioventricular (AV) node show a slowly depolarizing action potential.

As illustrated in figure 2.8, the cardiac action potential is subdivided into phases (0-4). Phase 0

designates the rapid upstroke of the action potential. Phase 1 mark a brief period of partial repolarization, followed by a plateau (phase 2) that persist for about 0.1 to 0.2s [10] Repolarization (phase 3) is a much slower process than depolarization (or phase 0). The interval from the end of repolarization until the beginning of the next action potential is phase 4, the resting membrane potential or, in the case of nodal AP, the diastolic depolarization.

2.3.3 Ionic basis of the fast response AP

If cell depolarization caused by an external or spontaneous (in pacemaking cells) stimulus is sufficient to raise the membrane potential above a critical value, the threshold potential, Na channels open, and further depolarize the membrane, initiating an action potential. In pacemaking cells, Na current is absent, excitation is mediated by activation of Ca currents [10].

In the fast response AP, the rapid depolarization (phase 0) is almost exclusively due to Na ions entering the cell and driving the membrane potential towards the Na Nernst potential, E_{Na} ($+65 - +70mV$). The Na currents activate very rapidly, 1 to 2ms [10]. The flux of Na ions through the channel is controlled by the activation gates of the Na channel. As the membrane potential becomes less negative, the inactivation gates close the channel [10]. These activation and inactivation gates are designated m and h gates respectively as originally coined by Hodgkin and Huxley [52]. The upstroke of the action potential falls short of E_{Na} because of inactivation of Na currents and activation of K current, the transient outward currents (Ito) which produce rapid membrane repolarization to +10mV (phase 1). Depolarization of the action potential also activates other currents, more slowly than the Na and Ito currents. In ventricular myocytes, Ical is activated and account for the major depolarizing current during the action potential plateau (phase 2). Influx of Ca^{2+} triggers Ca^{2+}-induced Ca^{2+} release (CICR) from the SR to initiate contraction [119]. The depolarizing effect of Ical is opposed by the activation of the delayed rectifier and inward rectifier repolarizing K currents (Ik, Ik1, Ito), active during the plateau and phase 3. Activation of the delayed rectifier K currents and inactivation of Ca currents serve to terminate the plateau phase and begin the late repolarization or phase 3. Final repolarization is mediated by the outward component of Ik, Ik1

inward rectifier. The ionic concentration is restored by the Na-K ATPase, the Na/Ca exchanger and the ATP-driven Ca pump. The NaK ATPase remove the excess Na that entered the cell rapidly during phase 0 and move slowly through the AP [10]. This pump eject Na in exchange for K that had exited mainly during phase 2 and 3. The Na-Ca exchanger exchange 3 Na for 1 Ca, whereas a fraction of Ca is eliminated by ATP-driven Ca pump.

2.3.4 Excitability and refractoriness

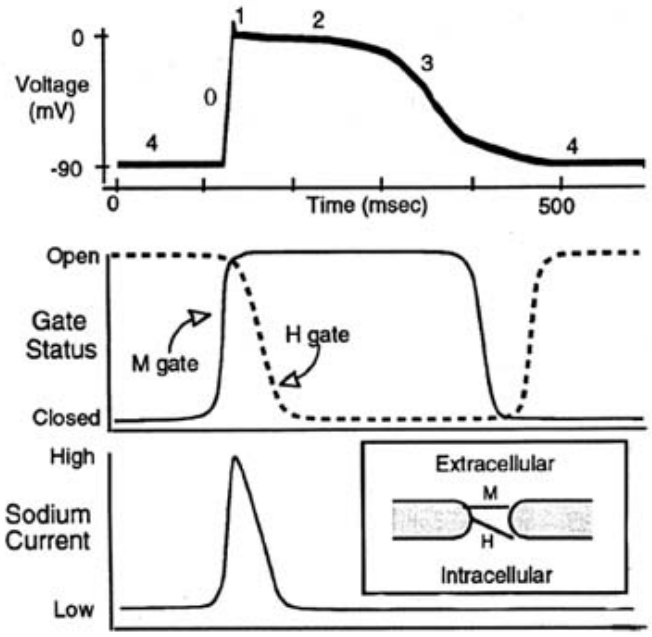

Figure 2.9: Action Potential and Sodium gating
Both activation(m) and inactivation(h) gates must be open for Na current to flow
At rest, nearly all the m gates are closed while the h gates are open; G_{Na} is very small and I_{Na} is minimal

The ability of a cell to respond to an external stimulus by depolarizing and forming an AP is known as excitability. The excitability of a cell depends on many factors, but most importantly on the availability of the sodium channel. The states of the sodium activation and inactivation gates (m and h) is voltage and time dependent.

Upon electrical stimulation of a cell (either from an external electrode or from an adjacent cell), the membrane potential becomes more positive and opens the Na channels (opens the m gates),

allowing Na ions to enter the cell causing the cell to further depolarize and the membrane potential shift to more positive potential. At the same time, the h gates begin to close to prevent further Na influx; both gates are open for only a few milliseconds (see figure 2.9). Once the h gates close, Na influx stops no matter how large a stimulus is applied. The cell cannot reopen the channel to generate another AP. The cell is, at that time, refractory. Refractoriness is a property of cardiac cells which results in a minimum time between electrical excitations [119].

During phases 2 and 3 of the AP, the m and h gates gradually recover their ability to respond. A stimulus applied near the end of phase 3 can open only those channels whose h gates have returned from the open state. If not enough channels are opened to allow sufficient Na influx to result in a regenerative depolarization of the cell, the cell is in an absolute refractory period. If a stimulus arrives a few milliseconds later when more h gates have recovered, enough channels will have been opened to conduct some Na current but not a normal amount. This gives rise to a slower upstroke to phase 0 and is termed the relative refractory period. Stimuli showing up still later encounter almost all the gates at the ready state, and a normal AP results, fully excitable (see figure 2.10).

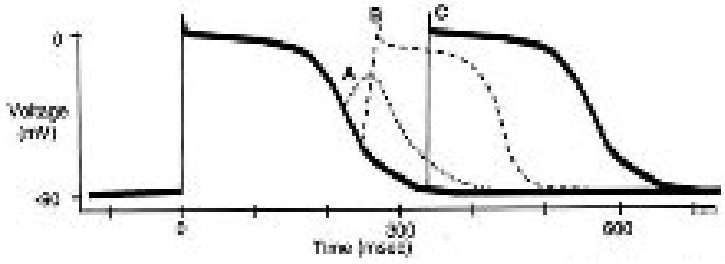

Figure 2.10: A stimulus applied to a cell before recovery of a critical number of Na^+ channels fails to generate another action potential (A)-the absolute (effective) refractory period. A slightly later stimulus finds enough Na^+ channels ready to yield an action potential, but with a delayed upstroke (B)- the relative refractory period. The action potential in C is the result of a stimulus applied after full recovery of the mass of Na^+ channels.

2.4 Propagation in the cardiac cellular network

An impulse generated in the sinoatrial node propagates rapidly through atrial and ventricular myocardium to coordinate excitation and contraction of the working myocardium. An abnormal site of impulse initiation or an abnormal pathway of impulse propagation (i.e, propagation slowing and propagation block) can result in reentrant rhythms, a self-perpetuating pattern of propagation which is the mechanism of maintenance of most cardiac tachyarrhythmias [64].

Cardiac muscle cells, which are $30-100\mu m$ long and $8-20\mu m$ wide with an irregular staircase shape, are typically connected to 10 neighboring cells [53] via gap junctions. Because of the low conductivity of the cell membrane and the spatial organization of the connexons (preferentially located at the cell ends), current flows more rapidly in the direction parallel to the longer cell axis (the longitudinal direction) than it does in the perpendicular (transverse) direction. This organization results in anisotropic electrical properties in which the average conductivity is greater longitudinally than transversely [23]. At the cellular level, electrical anisotropy is affected by the shape and the size of the cells, the amount and the distribution pattern of gap junctions [64]. Pathological changes in cell size (cell swelling) as well as changes in the interstitial (extracellular) volume affect conduction velocity by modifying the interstitial resistance to current flow, and therefore also affect anisotropy [40].

2.4.1 Source-Sink Relationship

Action potential propagation is usually thought of in terms of sources and sinks [64]. An excited cell serves as a source of electric charge for depolarizing neighboring unexcited cells towards their excitation threshold. The unexcited cells constitute an electric sink (load) for the excited cell. For successful propagation, the excited cell (the source) must provide sufficient charge to the unexcited cells (the sinks) to bring their membrane to excitation threshold and therefore generate an action potential. The newly excited cell switches from being a sink to being a source for the downstream tissue, perpetuating the process of action potential propagation.

2.4.2 Safety Factor

The Safety factor for propagation (SF) is a dimensionless parameter aimed at quantifying the source-sink relationship and it is useful to measure the success of propagation. It indicates the margin of safety with which the action potential propagates relative to the minimum requirements for sustained conduction [108]. The safety factor for conduction (SF) is generally defined as the ratio of charge generated for the fiber by cell excitation to the minimal amount of charge required to cause cell excitation [108]. A SF greater than 1 indicates that more charge was produced during cellular excitation than charge required to cause excitation. The fraction of SF above 1 indicates the margin of safety. When SF falls below 1, the charge requirements are not met and conduction fails.

2.4.3 Slow Conduction and Block

In many pathological conditions a decrease in cellular excitability, cellular uncoupling, or the development of structural heterogeneities can lead to slow conduction and the initiation of cardiac arrhythmias [64]. (It should also be noted that slow conduction occurs during propagation of a normal cardiac impulses through the atrioventricular node.)

Reduced excitability is mainly due to reduced availability of Na^+ channels, leading to a reduction in I_{Na}. Such a condition is usually present during acute or sub-acute ischemia [66]. Reduced sodium channel availability causes the cell to have an action potential with a slower upstroke and therefore a slower conduction velocity and a reduced SF [108]. When SF falls below 1, conduction cannot be sustained and block occurs [108].

Physiologically, atrial and ventricular myocardial cells are well-coupled However, in pathological conditions like ischemia, rapid cell-to-cell uncoupling may occur. Changes in the amount of Cx43 expression or cellular distribution patterns of gap junctions may result in reduced intercellular coupling [20]. Conduction velocity decreases monotonically with reduction in intercellular coupling, whereas SF increases to a maximum as coupling is reduced and velocity is significantly slowed [108]. With this high SF, extremely slow conduction velocities can be sustained in tissue with greatly reduced intercellular coupling [64, 99]; a very large reduction of intercellular coupling

is required to cause major slowing of conduction. Further decreases in cell coupling will inevitably result in conduction block [108].

Extremely slow conduction due to discontinuous tissue structures were observed in the center of the atrioventricular node [11, 12, 76] and in tissue surviving myocardial infarction [30, 29]. In the atrioventricular node, dead end pathways were found emerging from the center of the node. These pathways do not participate directly in the atrioventricular or ventriculoatrial impulse transmission and are activated later than the central portion of the node. After myocardial infarction, dead tissue causes ziq-zagging of conduction resulting in very long pathway of propagation with an effective very slow conduction velocity [30].

Chapter 3

Modeling Cardiac Electrophysiology

3.1 Modelling Cellular Excitation

Knowledge concerning the electrophysiology of the heart, precursor of cardiac mechanical contraction, is necessary for the understanding of cardiac physiology and pathophysiology. Substantial experimental measurements have delivered data of cardiac electrophysiological quantities from specific regions and from the whole heart. The delivered experimental data may include; potential measurement across spatial domains, like the cell membrane; flows and concentrations of ions in the intra-, extra-, and intercellular compartments; geometrical and functional characteristics of myocytes; extracorporal registration of electrocardiogram, etc. However, most of the collected data are from isolated preparations very different from the cardiac cell environment where these ion channels function physiologically. Therefore, a need to an integrative system that reproduces the electrical behavior of the cardiac tissue.

Computer modeling and simulation have shown strong suitability in integrating these dynamic processes involved into the generation and propagation of the cardiac action potential. Models were first based on ionic processes, carefully formulated mathematically using experimental data. An integrated combination of cell dynamic models (i.e ionic processes, membrane patches) describe the electrophysiological status of the cell both qualitatively and quantitatively, as observed experimen-

tally. New experimental data and advancement of computers have brought about more sophisticated formulations that include calcium transport mechanism, ATP production, metabolic pathways, and tissue structures. These modeling approaches, reproducing the electrophysiology of single cell or cell clusters, allow the generation of hypotheses on how changes in the function or structure of the integral mechanism affect the electrical properties of the whole cell or vise versa. They also may provide insight into some physiological and pathophysiological aspects of the heart.

3.1.1 Modeling the Cell Membrane as Resistor-Capacitor Circuit

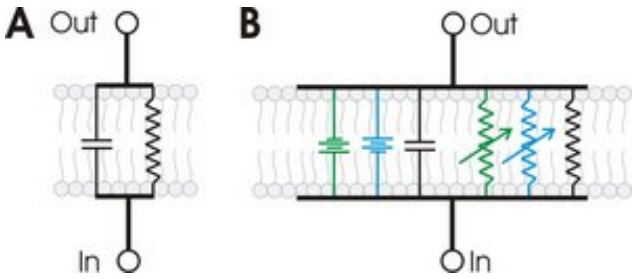

Figure 3.1: A:The electrical properties of the cell membrane modeled as a resistor-capacitor circuit.
The capacitor (C) represents the capacitance of the lipid bilayer that forms the cell membrane, the resistor (R) represents the conductance of the ionic channels that are open at the resting membrane potential.
B: The equivalent Hodgkin-Huxley model
Modified from [104]

In 1938 Curtis and Cole [27] measured the resistance and capacitance in nerve cells. They demonstrated that the electrical properties of the cell membrane could be modeled as a resistor-capacitor circuit (see figure 3.1)

They showed that cells have a high-conductance cytoplasm that is surrounded by a high resistance membrane with an electrical capacitance of about $1\mu F/cm^2$. The capacitor represents the capacitance of the lipid bilayer that forms the cell membrane, and the resistor represents the conductance of the ionic channels that are open at the resting membrane potential. The voltage across the membrane, Vm, depends on the charge Q:

$$V_m = \frac{Q}{C_m} \tag{3.1}$$

Change to the transmembrane voltage Vm can be described by the current flow Ic;

$$\frac{dV_m}{dt} = \frac{d}{dt}\frac{Q}{C_m} = \frac{I_c}{C_m} \qquad or \qquad C_m * \frac{dV_m}{dt} = I_c \tag{3.2}$$

Eq.(4.2) is the foundation of most electrophysiological models of cell membrane.

3.1.2 The Hodgkin and Huxley formulation

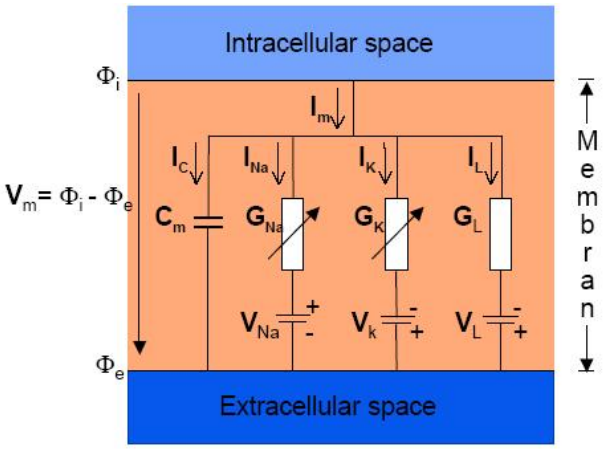

Figure 3.2: The parallel conductor model as developed by Hodgkin and Huxley
The sodium and potassium channels are both voltage-gated. An ungated channel, a generic leak current represented the collective contribution of other ions.
Modified from [104]

Hodgkin and Huxley (HH) [52] developed a mathematical description of the electrophysiological dynamics of the giant squid axon membrane based on experimental measurements. They measured the electrical behavior of the cell membrane to parametrize an equivalent R-C circuit. HH found that the major components of the squid giant axon's action potential were the sodium and potassium currents. Both channels are voltage-gated and open in a time-dependent manner following depolarization of the membrane. They also included an ungated channel, a generic leak current representing the collective contribution of ions such as chloride and bicarbonate. Figure 3.2 illustrates the circuit diagram depicted by HH.

The total transmembrane current, Im, is derived from Ohm's law (using (4.2)):

$$I_m = C_m * \frac{\partial V_m}{\partial t} + \sum I_{ion} \tag{3.3}$$

Where C_m is the membrane capacitance, I_{ion} is the current associated with a given ion. From Kirchhoff's first law, the sum of currents into and out of a cell is zero ($I_m = 0$), hence (4.3) can

be rewritten as

$$\frac{\partial V_m}{\partial t} = -\frac{1}{C_m} * \sum I_{ion} \tag{3.4}$$

Each of the ionic currents (I_{Na}, I_k, I_l) can be modelled as a function of ion conductance (g_{ion}), transmembrane voltage (V_m), and the ion equilibrium potential (E_{ion}):

$$I_{ion} = g_{ion} * (V_m - E_{ion}) \tag{3.5}$$

The equilibrium potential (E_{ion}), also known as the ion reversal potential, is the voltage required to oppose the concentration gradient induced ion flow; E_{ion} depends on the gradient between the intracellular and extracellular concentration of a given ion: $[Ion]_i$ and $[Ion]_e$, respectively. Walther H. Nerst [81] described this relationship as an equilibrium voltage of the cell membrane:

$$E_{ion} = \frac{R.T}{Z_{Ion}F} ln \frac{[Ion]_e}{[Ion]_i} \tag{3.6}$$

Where R is the universal gas constant ($R = 8314.4 mJ.mol^{-1}K^{-1}$), T is the absolute temperature in Kelvin ($T = 300^o K$, at body temperature), Z_{Ion} is the valence of the ion, and F is the Faraday constant ($F = 96484.6 C.mol^{-1}$).

Hodgkin and Huxley developed a series of equations based on empirical descriptions to model the behavior of the sodium and potassium conductance as a function of time and voltage, while that of the leak current is constant. They modelled the ion conductance (g_{ion}) using a maximum conductance, ($\overline{G_{ion}}$), and an activation gate, n, ranging from 0 to 1:

$$g_{ion} = \overline{G_{ion}}.n \tag{3.7}$$

Figure 3.3 illustrates the gating mechanism regulating the movement of ions. The gating is, in turn, regulated by specific stimuli; voltage, mechanical stress, or binding of a ligand.HH treated gating as a stochastic process; channels can either be in two states: opened or closed. Transition between the two states is a rapid process with a negligible number of channels in transition. If the

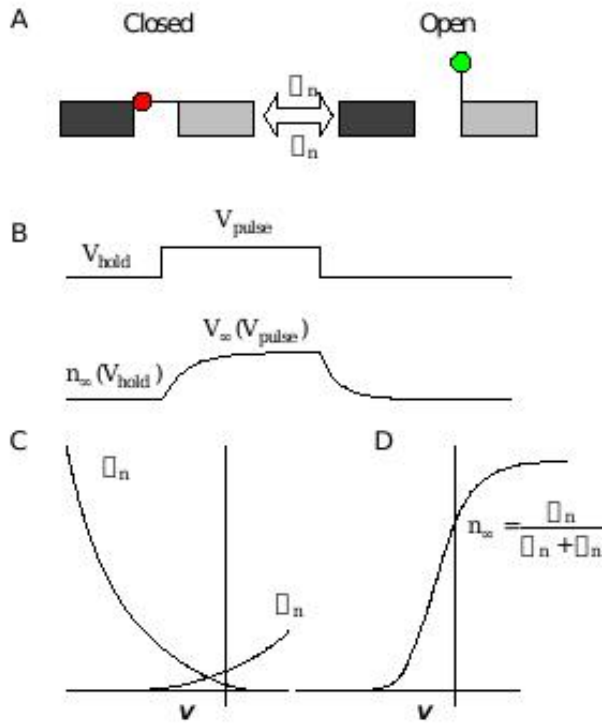

Figure 3.3: Gating mechanism regulating ion movements with open and closed states

probability (or fraction) of open channel is n, then the probability of closed channel is $(1-n)$. The channel is controlled by gates that move between two states with an opening rate coefficient α and a closing rate coefficient β. Both coefficients are time and voltage dependent. The rate of opening is thus given by $\alpha(1-n)$ and the rate of closing is βn. Then the net rate of change n of open channel is given by the difference in the rates of opening and closing:

$$\frac{dn}{dt} = \alpha_n.(1-n) - \beta_n.n \tag{3.8}$$

At steady state, the rate of change of open channels is zero ($\frac{dn}{dt} = 0$) therefore (3.8) can be formulated as:

$$\frac{dn}{dt} = \frac{n_\infty - n}{\tau_n} \tag{3.9}$$

where n_∞ and τ_n are the steady state value and time constant of n respectively. They are also time

and voltage dependent and defined as follow:

$$n_\infty = \frac{\alpha_n}{\alpha_n + \beta_n} \qquad and \qquad \tau_n = \frac{1}{\alpha_n + \beta_n} \tag{3.10}$$

(3.9) can be integrated to give n as a function of time

$$n(t) = n_\infty - (n_\infty - n_o).\exp(-\frac{t}{\tau_o}) \tag{3.11}$$

The gating variable n can be raised to the power p (n^p) if there are p gates in series in one ion channel, i.e if the channels goes through different states between the open and close states. Channels can also be given more than one gate variable (gate particle) to describe activation-inactivation behavior. These independent gating particles would have to be in the correct state to allow current to flow. The experimental data was used to approximate the proper conformation of the gating variable for each channel. From the results, both the probability of opening the potassium and sodium channels rise in a sigmoidal manner rather than a simple exponential.

The potassium channel, which has only an activation particle, is best fitted with a 4 gating particles. Therefore n is replace by n^4 Thus the potassium current becomes:

$$I_k = \overline{G_k} n^4 (V_m - E_k) \tag{3.12}$$

The sodium current is more complex because it activates and inactivates. The channel activates in a sigmoidal manner and inactivates rapidly. The probability of the channel being open depends on the probability of the channel being activated, but also that it is not inactivated, so the gating particle requires two components. The sodium channel is best fitted with activation represented by three gating particles (m^3) and inactivation represented by one gating particle (h);

$$I_{Na} = \overline{G_{Na}} m^3 h (V_m - E_{Na}) \tag{3.13}$$

The leak current is not time dependent and thus can be categorised as a background current formulated as:

$$I_l = \overline{G_l}(V_m - E_l) \tag{3.14}$$

The rate constants α and β are functions of voltage but not of time. The expressions for the rate constants were found by fitting curves to experimental data from the nerve fibres to give:

$$\alpha_m = \frac{0.1(V_m + 25)}{e^{\frac{V_m + 25}{10}} - 1} \tag{3.15}$$

$$\beta_m = 4e^{\frac{V_m}{18}} \tag{3.16}$$

$$\alpha_h = 0.07e^{\frac{V_m}{20}} \tag{3.17}$$

$$\beta_h = \frac{1}{e^{\frac{V_m + 30}{10}} + 1} \tag{3.18}$$

$$\alpha_n = \frac{0.01(V_m + 10)}{e^{\frac{V_m + 10}{10}} - 1} \tag{3.19}$$

$$\beta_n = 0.125e^{\frac{V_m}{80}} \tag{3.20}$$

3.2 Cardiac Myocytes' models

3.2.1 The First generation cardiac models

Models of the cardiac membrane action potential were primarily developed from animal experimental data about the voltage and time dependence of ion channel conductances, see [102, 92] for review. These models use the mathematical formulations of Hodgkin and Huxley [52] with the following general form (reproduced from [22]).

$$C_m \frac{dV_m}{dt} = -\sum_S I_S \tag{3.21}$$

$$I_S = \overline{G_S} x_S^1 x_S^2 \dots x_S^n (V_m - E_S) \tag{3.22}$$

$$\frac{dX_S}{dt} = \frac{X_{S\infty}(V_m) - X_S}{\tau_S(V_m)} \tag{3.23}$$

Where I_S is the current carried by an ionic species S through a particular ion channel, $\overline{G_S}$ the maximal conductance for the ion channel, x_S are the gating variables describing the activation, inactivation and recovery of the ion channel, E_S is the Nernst reversal potential of species S, $X_{S\infty}$ and τ_S are the steady-state value and time constant of a single gating variable respectively (details on the different variables are given in the HH formulation above).

Thus a general membrane model comprises one equation imposing current conservation (3.21), some mass conservation equations describing the fluid compartment model, and some kinetic gating (3.22, 3.23). The common independent variable is time, the dependent variables are the transmembrane voltage, the ionic concentrations and the gating variables. All equations together constitute a system of first-order nonlinear ordinary equations (ODEs). Analytic solutions are not known for this sytem, numerical methods are therefore required.

The Noble Model

In 1962, Denis Noble [83] published the first mathematical models of a cardiac cell. The Noble model describes the long-lasting action and pace-maker potentials of the Purkinje fibers of the heart by modifying the Hodgkin Huxley equations. Figure 3.4 illustrates the model structure with its three ionic currents: N_a^+, K^+, and a leak current attributed in part to chloride ions.

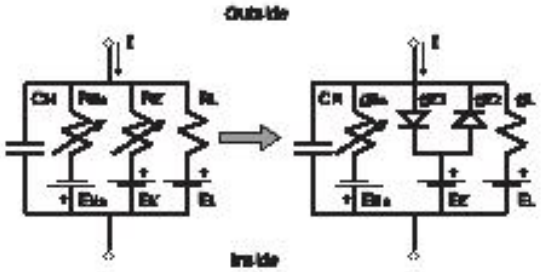

Figure 3.4: The basic Hodgkin and Huxley representation of the squid axon (left) was modified to represent the Purkinje cell (right). In the latter K^+ current is assumed to flow through two non-linear resistances.
Modified from [92]

The sodium current equations are very similar to those of Hodgkin and Huxley model [52] with

an added small component of g_{Na} ($0.14 mmho/cm^2$) independent of voltage and time;

$I_{Na} = g_{Na}(V_m - E_{Na})$

where $g_{Na} = \overline{G_{Na}} m^3 h + 0.14$, $\overline{G_{Na}} = 400 mmho/cm^2$, $E_{Na} = 40mV$,

with the following expressions for the rate constants:

$\alpha_m = (0.1(-V_m - 48))/(\exp((-V_m - 48)/15) - 1)$,

$\beta_m = (0.12(V_m + 8))/(\exp((V_m + 8)/5) - 1)$,

$\alpha_h = 0.17 \exp((-V_m - 90)/20)$,

$\beta_h = 1/(\exp((-V_m - 42)/10) + 1)$.

The potassium currents are assumed to flow through two types of channel in the membrane. In one channel, the potassium conductance g_{k1} is assumed to be an instantaneous function of the membrane potential and falls when the membrane is depolarized. In the other type of channel, g_{k2} slowly rises when the membrane is depolarized; it is time and voltage dependent [83]; $I_K = (g_{k1} + g_{k2})(V_m - E_K)$, with $g_{k1} = 1.2 \exp((-V_m - 90)/50) + 0.015 \exp((V_m + 90)/60)$, $g_{k2} = \overline{G_k} n^4$. Where $\overline{G_k} = 1.2 mmho/cm^2$, $E_k = -100mV$, $\alpha_n = (0.0001(-V_m - 50))/(\exp((-V_m - 50)/10) - 1)$, $\beta_n = 0.002 \exp((-V_m - 90)/80.0)$.

The McAllister, Noble and Tsien (MNT) Model

The next significant development in cardiac membrane modeling occurred when McAllister, Noble and Tsien [75] published a paper which formulated an updated Purkinje fibre model with new ionic current equations based on a mosaic of new experimental data. The description of the kinetics of the currents was still based on the Hodgkin-Huxley formalism, but the currents themselves incorporate some significant new changes, and the total ionic current is broken down into nine discrete, individual ionic fluxes: $\sum I_{ion} = I_{Na} + I_{si} + I_{qr} + I_{K2} + I_{x1} + I_{x2} + I_{K1} + I_{Na,b} + I_{Cl,b}$.

This model featured a role for Ca^{2+} in the generation of the AP (generated a secondary depolarization preceding the plateau), in the form of the secondary or slow inward current I_{si}; and a novel Cl^- channel, in the form of a transient outward current I_{qr} activated during strong depolarizations. The model also featured three separate time-dependent outward currents. the pacemaker K^+ current

I_{K2} and the time-dependent K^+ currents: the fast I_{x1} and the slow I_{x2} components of a new current observed at a higher voltage range (plateau potentials [75]) ; The leak current, described in HH as a small residual current that remains when the time-dependent currents are accounted for, is refered here as the background current. The total background current was composed of the outward K^+ current, I_{K1} ; the inward Na^+ current I_{Nab} and the current carried by Cl^- current, $I_{Cl,b}$.

The MNT model provided explanations for a wide variety of electrical behavior in the Purkinje fiber, including the chronotropic effect of external Ca^{2+} and adrenaline's acceleratory effects on pacemaker activity (with the latter described by incorporating the observed voltage-shift on the kinetic parameters of I_{K2} in response to adrenaline) [92].

The Beeler and Reuter model

The Beeler and Reuter model [8] describes the electrophysiology of a mammalian ventricular action potential based on measurements with the voltage-clamp method on multicellular preparations of cardiac muscle. This concise model consisted of only four ionic currents: $I_{K1}, I_{X1}, I_{Na}, I_{Ca}$ plus a stimuli current. The main additional feature of the Beeler-Reuter ionic current model is a representation of the intracellular calcium ion concentration, $[Ca^{2+}]_i$. The model took into account the function of Ca^{2+} as a link between electrical events at the membrane and the contractile responses of the cell. The connection between the membrane potential and changes in internal Ca^{2+} was bi-directional, so that $[Ca^{2+}]_i$ also influenced I_{Ca}. The handling of $[Ca^{2+}]_i$ was modeled as flowing into a small distribution volume within the cell, from which it was removed by an uptake mechanism which would reduce $[Ca^{2+}]$ in that compartment exponentially with time ($\tau = 70s^{-1}$) to achieve a resting level of $10^{-7}M$.

The Beuler-Reuter model adequately described some experimental phenomena like slow recovery of the sodium system from inactivation, frequency dependence of the action potential duration, all-or-none repolarization, and membrane oscillations.

The Luo and Rudy (LR1) Model

The first version of Luo and Rudy was introduced in 1991 [70] and was a successor of the Beeler and Reuter's description of the mammalian ventricular myocyte [8]. This model described the guinea-pig ventricular myocyte and introduced the dependence of K^+ currents on $[K^+]_o$ concentration, the negative-slope characteristics of the time-independent K^+ current (I_{k1}), a novel K^+ channel (I_{kp}) that activates at plateau potentials, and a reformulation of the fast Na^+ current, with I_{Na} inactivated by fast and slow processes. The total membrane current of the Luo-Rudy phase-1 model consist of: $\sum I_{ion} = I_{Na} + I_{si} + I_K + I_{K1} + I_{Kp} + I_b$.

This model allows the reproduction of supernormal activity, defined as larger than normal excitability during or after the repolarization phase, and of Wenckebach periodicity, defined as periodic, stimulus frequency dependent activation failure [104]. It has been extensively used for simulating action potential propagation in tissue [94]

3.2.2 The second generation cardiac models

These models add a detailed description of the intracellular Na^+, Ca^{2+}, K^+ concentrations to the biophysical description of ion channel, pump and exchanger currents developed in the primary models [22].

$$\frac{d[S]}{dt} = \sum_k I_S^k(V_m, S) \tag{3.24}$$

(3.24) describes the balance of ion S, the concentration of which is affected by k different types of ion channels, pumps and exchanger currents that are carrying this ionic species. An equation of this type is included for each ionic species.

The Difrancesco and Noble Model

Di Francesco and Noble [36] published a model that included what was then newly described mechanisms in addition to ionic currents, e.g., electrogenic pumps and intracellular calcium handling, see figure 3.5.

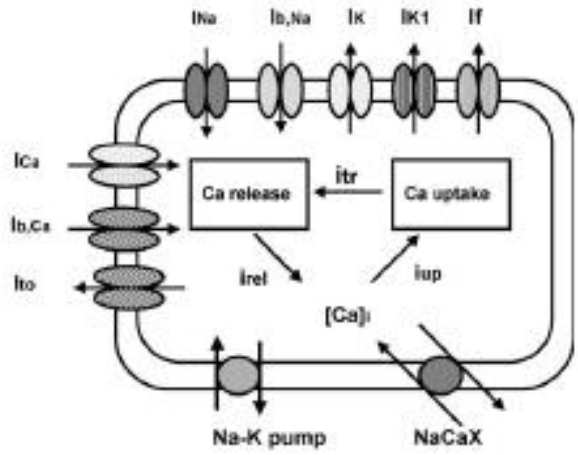

Figure 3.5: The Di Francesco and Noble model.
Besides the ionic currents it incorporated ionic pumps and exchanger mechanisms. It also included a description for C_a^{2+} movement inside of the cell. SR.
Modified from [92]

This model described the Purkinje fiber with an added formulations for the Na^+-K^+ pump (Na/K-ATPase) and Na^+-Ca^{2+} exchanger (NaCaX). The sarcoplasmic reticulum (SR) was represented by two compartments, including one for Ca^{2+} uptake, which then reprime a release store. Ca^{2+} induced Ca^{2+} release [38] was implemented assuming that the release was triggered by intracellular free Ca^{2+}.

External and internal ionic concentrations were now variables which enabled this model to successfully reproduce experimental results including [92]; (a) intracellular Na^+ concentration changes due to variations in $[Na^+]_o$ or Na^+-K^+ pump block, (b) the Na^+ dependence of the overshoot potential, (c) the shortening of AP duration at high $[K^+]_o$, (d) the increased automaticity at low $[K^+]_o$ and (e) the depolarization to the plateau range with premature depolarization and low voltage oscillations at very low $[K^+]_o$. This model was the first model available as a software package Oxsoft HEART (1984) [92]; allowing users to modify channel's conductance, alter ionic concentration or create their own stimulation protocol.

The Luo and Rudy phase 2 model

In 1994 The Luo-Rudy phase-2 model was introduced [72]. This model was an improvement of the first model which incorporates a more thorough description of the regulation of intracellular calcium ion concentration and the movement of calcium ions through the cell and to and from the

sarcoplasmic reticulum. Calculations of intracellular Na^+, K^+ and Ca^{2+} were possible at each step, due to the inclusion of pumps and an exchanger located in the membrane and a new description of the SR (compared to the MNT model). The SR model now consisted of a network SR (NSR) where the Ca^{2+} was taken up via a pump (I_{up}), and a junctional SR (JSR), to which this Ca^{2+} was then translocated following a mono exponential function, ($Irel$) [136]. Buffers were included in the cytoplasm (troponin and calmodulin) and the SR (calsequestrin) with steady-state kinetics, due to the slight differences obtained using dynamic buffering process and the improvement in the computational time.

The total membrane current of the original Luo-Rudy phase-2 model consist of:

$$\sum I_{ion} = I_{Na} + I_{Ca,L} + I_K + I_{K1} + I_{Kp} + I_{NaCa} + I_{NaK} + I_{ns(Ca)} + I_{p(Ca)} + I_{Ca,b} + I_{Na,b}$$

The next formulation of the Luo-Rudy model (Zeng et al. 1995) [136] permitted a better analysis of AP repolarization and restitution of the AP duration, with the delayed rectifier K^+ current split into a rapid I_{Kr} and a slow component I_{Ks} as well as the inclusion of T-type Ca^{2+} channel ($I_{Ca,T}$). The intracellular calcium mechanisms are governed by four currents: the Ca^{2+} uptake from myoplasm to NSR, I_{up}; the Ca^{2+} release from JSR, I_{rel}; the Ca^{2+} leakage from NSR to myoplasm, I_{leak}; and the Ca^{2+} translocation from NSR to JSR, Itr.

This model provided the basis for the study of arrhythmogenic single cell phenomena [92] such as the early afterdepolarization (EAD) which is a depolarizing after-voltage beginning before the completion, the delayed afterdepolarization (DAD), which is a depolarizing after-voltage beginning after the completion of the repolarization; as well as triggered and rhythmic activity. The model also provided means to simulate cellular responses under different degrees of Ca^{2+} overload [72]. This model was a framework for modeling other types of ventricular cells with appropriate modifications made to account for species differences.

Different models for different species and different cell types

In the mid 1990s, electrical physiological studies have shown species differences in the action potential waveforms and ionic currents [105, 125, 33, 7, 90]. Gender differences [122] and

regional heterogeneities [5] were noticed as well. Modeling then shifted from integrating voltage-clamp data from several species to species-dependent modeling; accounting for gender and regional heterogeneities as necessary.

Several species-dependent models have been developed: rabbit sinoatrial (SA) node model [137, 85], rabbit ventricular model [91], rat models [32, 86, 87], canine ventricular cell model [130, 45], canine atrial model [96, 65], canine epicardial cell [18]. Human myocyte models has proven elusive due to the lack of extensive experimental data for validation. Few human models were published [84, 25, 89].

The Cabo Boyden Epicardial Border Zone Model

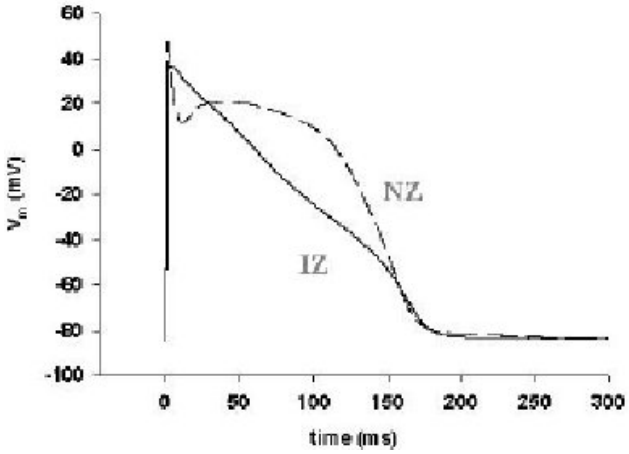

Figure 3.6: Computer model of an action potential of a cell isolated from the epicardial border zone (IZ, solid), and a cell isolated from normal epicardium (NZ, dashed) [18]

In this thesis, we use the ionic model of canine epicardial cells developed by Cabo and Boyden [18]. They measured and parametized ionic models of canine epicardial cells. They developed ionic model for both normal cell (NZ) and cell surviving the infarct (IZ). Currents were formulated by fitting mathematical functions to voltage-clamp experimental measurements following Hodgkin-Huxley formalism [52]. These currents include the Na^+ current I_{Na}, I_{CaL}, transient outward K^+ current I_{to}, delayed rectifier K^+ currents I_{Kr} and I_{Ks}, inward rectifier K^+ current I_{K1}, and Na^+/Ca^{2+} exchanger current I_{NaCa}. Currents that have not been completely characterized in IZs ($I_{Kp}, I_{NaK}, I_{nsCa}, I_{Cab}, I_{Nab}$) were adopted from the formulation proposed by Luo and Rudy [71].

The total membrane current was therefore: $\sum I_{ion} = I_{Na} + I_{CaL} + I_{to} + I_{Kr} + I_{Ks} + I_{K1} + I_{Kp} + I_{NaCa} + I_{NaK} + I_{nsCa} + I_{pCa} + I_{Cab} + I_{Nab}$

Figure 3.6 shows simulated action potentials generated with the NZ and IZ models. The loss of plateau in the triangular shaped action potential of the IZ cell model [69, 123] was faithfully reproduced. These models have been used to explain paradoxical experimental results like a differential effect of antiarrhythmic drugs in NZ and IZ cells [18].

3.3 Tissue-level models of excitation propagation

To model the excitation propagation in the myocardium, we need descriptions of both the intrinsic membrane properties and the tissue structure i.e. how the cells are arranged or connected [50]. Different modeling approaches can be distinguished based on the representation of the microscopic and macroscopic anatomy as well as depending on the approximation of the cellular electrophysiology [104]. Macroscopic based models allow the combining of cells and their common treatment. Modeling approaches that use only macroscopic information include rule based(or cellular automata) and reaction diffusion systems. Microscopic based models split cells in components, which are separately treated [104].

3.3.1 Cellular Automata Model

Cellular automata as discrete models for propagation in cardiac tissue was introduced by Wiener and Rosenblueth [129], to describe phenomena of excitation propagation in two-dimensional sheets of cardiac muscle, and by Moe et.al [78] to model atrial fibrillation.

Cellular automata is the simplest approximation of propagation in cardiac tissue, where nodes (cells) arranged in a grid can exist in a number of discrete states, and the state of a particular cell is determined by a set of rules updated at successive time steps [22].

Cellular automata models are computationally efficient due to their simplified discrete model of propagation. However, they fail to reproduce some features of propagation and some electrophysi-

ological details.

3.3.2 Reaction Diffusion Model

Reaction diffusion systems, also known as excitable dynamics equations, use a system of non-linear partial differential equations (PDE) to describe the excitation and propagation process in excitable media [104]. The impedances that results from the conductivities of the intracellular sarcoplasm and extracellular fluid, the cell-to-cell coupling conductance and the membrane conductance and capacitance are spatially distributed, and so can be described by partial differential equations. These PDE models, described by simple equations or biophysically detailed models, provide the dominant computational approach to wave propagation phenomena in cardiac tissue. They involve the description of excitation propagation using the cable equation, coupled with detailed electrophysiological models of single myocardial cells. For a full review of these modeling approaches see [97, 57, 42]. For what follows, we present a summary of fundamental relations.

The cable equation (one dimensional fiber)

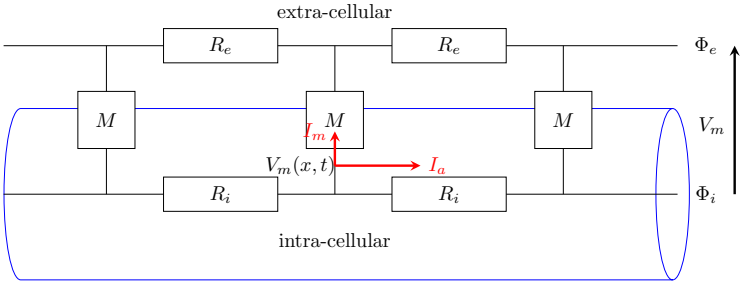

Figure 3.7: The cell as a one-dimensional cable with a conductive interior (Cytoplasm) surrounded by an insulator (cell membrane) with an axial current I_a, a membrane current I_m, intra and extra-cellular resitances R_i and R_e. R_e is usually neglected compared to R_i ($R_e = 0$ or $V_m = \Phi_i$).

Cardiac tissue behaves as a functional syncytium [126, 21] and so can be considered as a continuous medium. The cell membrane is conceived of as cylindrical boundary of finite thickness separating the intra-cellular and extra-cellular fluids. Axial symmetry is assumed, and the current flow inside the fiber is one dimensional, currents in the inner and outer conductors will flow in the longitudinal (x) direction only. Transmembrane current flows in the radial (r) direction only, see

figure 3.7.

The cable equation is derived from figure 3.7 using Ohm's law and conservation of charges respectively:

$$\partial V_m/\partial x = -RI_a \tag{3.25}$$

$$I_m = -\partial I_a/\partial x \tag{3.26}$$

Combining these two equations, we obtain:

$$\frac{\partial^2 V_m}{\partial x^2} = -\frac{\partial I_a}{\partial x} = RI_m \tag{3.27}$$

Where the membrane current (I_m) is both capacitive and ionic, $I_m = I_c + I_{ion}$, with I_c given by (4.2). (3.27) can therefore be written in the following form:

$$\frac{\partial V_m}{\partial t} = -\frac{1}{C_m} I_{ion} + \frac{1}{C_m R}\frac{\partial^2 V_m}{\partial x^2} \tag{3.28}$$

which represent the one-dimensional fiber model or cable equation of excitation propagation in cardiac tissue.

Two-dimensional tissue model

Cardiac tissue can be modeled as a two-dimensional sheet by extending the above result into a two-dimensional cable theory. Figure 3.8 shows a network of resistors that approximate the two-dimensional tissue model. A model of excitability describes the properties of each patch of membrane (the membrane boxes in the middle). The grid of resistors at the bottom (bottom sheet) represents the intracellular space and connects each membrane patch to its neighboring patches. These resistors take into account the resistance within each cell and the resistance of the intercellular channels. The top grid, on the other hand, represents the extracellular space [100]. Multi-dimensional models allow to account for the anisotropy of cardiac tissue which gives rise to a faster conduction velocity along than across the fiber.

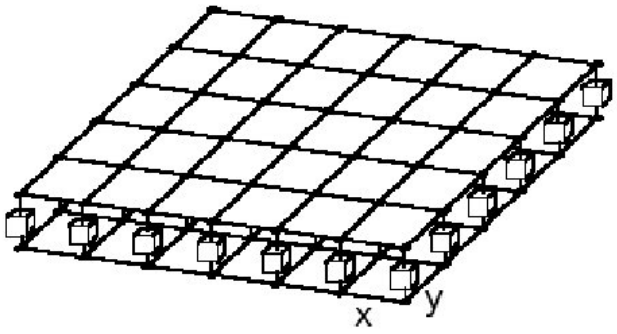

Figure 3.8: A network representation of the 2-D sheet.
The lower grid represent the electrical properties of the intracellular space with resistors, R_x and R_y
The membrane elements represent the membrane capacitance in parallel with the conductance of active ion channels.
The top grid represent the electrical properties of the extracellular space (modified from [82])

Monodomain Model

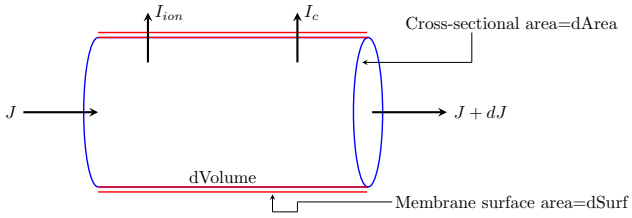

Figure 3.9:

The monodomain model provides the simplest description of action potential propagation. The extracellular potential is grounded(i.e. $\Phi_e = 0mV$), see figure 3.7, which means that the transmembrane potential is effectively equal to the intracellular potential ($V_m = \Phi_i$). The derivation of the monodomain equation can be done by expanding the cable equation to a multi-dimensional fiber, see figure 3.9. The electric field vector E (mV/cm) is defined as:

$$E = -\nabla\Phi \quad \text{with} \quad \nabla = \frac{\partial\hat{i}}{\partial x^2} + \frac{\partial\hat{j}}{\partial y^2} \tag{3.29}$$

where ∇ is the gradient operator (here for two-dimensional tissue). Ohm's law implies that current density is proportional to the electric fiel vector E:

$$J = DE = -D\nabla\Phi_i = -D\nabla V_m \tag{3.30}$$

Where J ($\mu A.cm^{-2}$) is the flux vector, D is a coefficient with units of distance^{2}time^{-1} that describes

the effective diffusion of voltage through the medium. For models of isotropic tissue D is a scalar quantity;

$$D = \frac{1}{S_v R_i C_m} = \frac{G_i}{S_v C_m} \tag{3.31}$$

Where S_v is the surface volume ratio of cells, R_i the bulk cytoplasmic resistivity of the tissue, C_m the specific capacitance and G_i the bulk intracellular conductivity.

Applying conservation of charge into figure 3.9 implies:

$$J.dArea - (J + d.J).\text{dArea} = (I_c + I_{ion})\text{dSurf} \quad \Rightarrow \quad -d.J.\text{dArea} = (I_c + I_{ion})\text{dSurf} \tag{3.32}$$

Where dArea is the cross section area, dSurf is the membrane surface area. Evaluating the left hand side of (3.32), we obtain:

$$-(\nabla.J)\text{dVolume} = (\frac{\partial V_m}{\partial t} + I_{ion})\text{dSurf} \tag{3.33}$$

Where we used (4.2) for I_c. Replacing J with (3.30), we obtain the monodomain model of action potential propagation:

$$\nabla.D\nabla V_m = \frac{\partial V_m}{\partial t} + \frac{1}{C_m} I_{ion} \tag{3.34}$$

The surface to volume ratio ($S_v = dSurf/dVolume$) is incorporated in the expression of D (3.31).

The monodomain model in (3.34) neglected the extracellular effects in its derivation. This makes it less computing intensive, as compared to the bidomain model. However, it still provides sufficient informations in most investigations of cardiac action potential propagation. In this thesis, we solved and implemented the monodomain model for all simulations.

Bidomain Model

In contrast to the monodomain model described above, the bidomain model treats the heart as having two continuous domains occupying equal volume; intracellular and extracellular, see figure 3.7. The transmembrane potential is the difference between the intracellular and extracellular

potentials:

$$V_m = \Phi_i - \Phi_e \tag{3.35}$$

Each domain has a flux:

$$J_i = -D_i \nabla \Phi_i \qquad J_e = -D_e \nabla \Phi_e \tag{3.36}$$

Where i and e denote the intracellular and extracellular spaces, respectively. The flux on each side of the membrane are equal and of opposite signs, since any current that leaves one space must reach the other through the cell membrane. The change in flux in each space must also be equal to the transmembrane current I_m. It therefore results that:

$$I_m = \nabla . J_i = -\nabla . J_e \qquad \text{or} \qquad S_v(C_m \frac{\partial V_m}{\partial t} + I_{ion}) = \nabla . J_i = -\nabla . J_e \tag{3.37}$$

Using (3.36) into (3.37), we obtain:

$$-\nabla .(D_i \nabla \Phi_i) = \nabla .(D_e \nabla \Phi_e) \tag{3.38}$$

To add $\nabla .(D_i \nabla \Phi_e)$ on both side of (3.38) and use (3.35) yields the first equation of the bidomain model, which describes the conservation of current across the intracellular and extracellular domains:

$$\nabla .(D_i \nabla V_m) = \nabla .((D_i + D_e) \nabla \Phi_e) \tag{3.39}$$

To compute this equation, the current flow in either domain needs to be determined. From (3.37) we obtain:

$$S_v(C_m \frac{\partial V_m}{\partial t} + I_{ion}) = \nabla .(D_i \nabla \Phi_i) \tag{3.40}$$

Then, like above, we add $\nabla .(D_i \nabla \Phi_e)$ on both sides of (3.40) and use (3.35) to remove any reference to Φ_i, leaving V_m and Φ_e, to obtain the second equation of the bidomain model:

$$S_v(C_m \frac{\partial V_m}{\partial t} + I_{ion}) = \nabla .(D_i \nabla V_m) + \nabla .(D_i \nabla \Phi_e) \tag{3.41}$$

This bidomain system consist of coupled parabolic and elliptic differential equations. These equations are much more difficult to numerically integrate than the monodomain equation because the full elliptic problem must be solved for each time step of the parabolic equation.

3.3.3 Microscopic Model

The modeling approaches depicted in the previous section enable large scale computations of action potential propagation, with good agreement between experimental studies. However, details of the arrangement of cardiomyocytes, their irregular shapes, and the nonuniform distribution of their gap junctions have not entered into the analyses and development of these models. These models represent cells as uniform cylinders. Whereas cardiac tissue is better described as an electrical network of complex geometry and discontinuous distribution of electrical parameters. The above approach, rather than modeling individual cells, models lumps of cells by averaging the electrical properties of the cells that are to be modelled. Averaging is done over a space scale bigger than the size of a single cell.

Spach et al [115] discovered that there are recurrent microscopic discontinuities due to cellular interconnections that alter the apparent load a cell ”sees” as the direction of propagation is changed, causing propagation to fail. This suggested that at microscopic level, cardiac conduction is discontinuous in nature. As noted by the authors [115], their findings provided a major departure from the long-held idea that cardiac muscle behaves as a continuous syncytium. They introduced microscopic models, where cells are split in components and are separately treated [110, 116]. By subdividing a cell into several segments, junctional resistances can be added at the terminal segments of the cell where the gap junction are assumed to be located [35, 49, 101, 131]. Thus the regular resistive network obtained from the continuous modeling approach can be adjusted to reflect variation in junctional coupling as well as cell geometry (cell size and shape) [110, 116]. Such modeling approach, however, is difficult and limited to small networks by the computational demands. Nevertheless, these models have shown that the propagation of action potentials is, at the cellular level, a stochastic process that may be important in suppressing some cardiac arrhythmias [110, 116].

3.4 Numerical techniques

The resolution of cardiac electrophysiological model consists of solving a reaction-diffusion problem. Where the reaction part involve the single cell model and the diffusion part solves the monodomain or bidomain model.

3.4.1 Cell model ODEs

The reaction part is aimed at solving the intrinsic behaviour of a single cell and determining its membrane potential, which is then used for computing the diffusion part. (3.21) together with the gating variables described by the voltage-dependent terms $x_{S\infty}(V_m)$ and $\tau_S(V_m)$ (3.23), describe the single cell model. Methods to solve these equations involve finite difference solution schemes including explicit Euler, fourth-order Runge-Kutta and implicit techniques [127]. In this thesis, we used the discrete-form proposed by Rush and Larsen [103]:

$$x_S^{t+1} = x_{S\infty}(V_m) + (x_S^t - x_{S\infty}(V_m))e^{-\Delta t/\tau_S(V_m)}. \tag{3.42}$$

Here V_m is the membrane voltage at time t, x_S are the gating variables described in the cell model section, and Δt is the time step. At each time step, the membrane currents, described by equations of the form (3.22), can be computed, and the new value of membrane voltage can be calculated from (3.21).

3.4.2 Finite difference solutions to the monodomain tissue model

In The diffusion part,we solve the monodomain equation using the finite difference method (FDM) [62]. Other approaches have been used; including methods based on finite elements [6],finite volumes [47], and combinations of these [13]. Also, the complexity of any of these numerical techniques is affected by the type of approach (monodomain or bidomain).

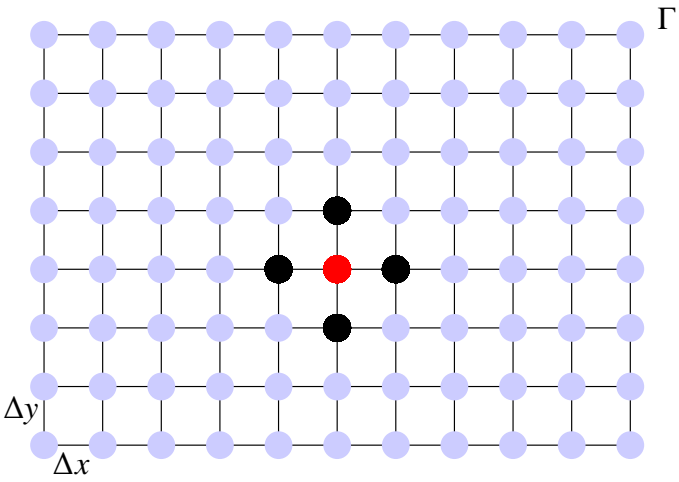

Figure 3.10: Finite difference mesh for a given domain(Γ). The mesh is made of grid points that lay within the domain and are equidistance from each other in both x and y direction (Δx and Δy, respectively).

Discretization

Figure 3.10 shows the discretized two-dimensional monodomain model as a network of resistors on a regular grid [48]. The diffusion and reaction parts of the model can be written respectively as:

$$\nabla.(D_i \nabla V_m(t, \mathbf{x})) = \frac{\partial V_m(t, \mathbf{x})}{\partial t} + \frac{1}{C_m} I_{ion}(V_m, x_S) - I_S(t, \mathbf{x}) \tag{3.43}$$

$$\frac{dx_S}{dt} = \frac{x_{S\infty}(V_m) - x_S}{\tau_S(V_m)} = f(V_m, x_S), n = 1, \ldots, N \tag{3.44}$$

Where $V_m(t, x)$ is the membrane potential at time t and location $\mathbf{x} = (x, y)$, $I_S(t, \mathbf{x})$ a stimulus current per unit volume to initiate propagation. The initial values of $V_m(t_o)$ and $x_S(t_o)$ are typically computed by assuming steady-state conditions $dV_m/dt = dx_S/dt = 0$. The reaction part (3.44) is the system of ODEs solved by (3.42) described in the previous section.

To solve the diffusion part (3.43), we rely on the finite difference mesh representing the two-dimensional sheet of tissue with domain $\Gamma = [0, a] \times [0, b]$, figure 3.10. Γ is definded as a set of nodes (x_i, y_j) with $\{x_i | x_i = i\Delta x, i = 0 \ldots N_x\}$ and $\{y_j | y_j = j\Delta y, j = 0 \ldots N_y\}$ representing a mesh with N_x segments along and N_y segments across the fibers, each segment of size $\Delta x \times \Delta y$ with $\Delta x = a/N_x$ and $\Delta y = b/N_y$. We seek approximation of the solution V_m defined everywhere in Γ at the mesh points (x_i, y_j) and denote it $V_{i,j}$. The diffusion term, given in the left hand side of (3.43) can be

writen in cartesian coordinates as:

$$\nabla.(D_i \nabla V_m(t, \mathbf{x})) = D_{iL} \frac{\partial^2 V_m(t, \mathbf{x})}{\partial x^2} + D_{iT} \frac{\partial^2 V_m(t, \mathbf{x})}{\partial y^2} \tag{3.45}$$

Where D_i is a diagonal matrix $diag(D_{iL}, D_{iT})$ with D_{iL} and D_{iT} designating the conductivity along and across the fiber respectively. The spatial operators in (3.45) can then be approximated by the finite difference method as follow:

$$D_{iL} \frac{\partial^2 V_m(t, \mathbf{x})}{\partial x^2}\Big|_{i,j} \approx D_{iL}\Big[\frac{V_{i-1,j} - V_{i,j}}{\Delta x^2} + \frac{V_{i+1,j} - V_{i,j}}{\Delta x^2}\Big] \tag{3.46}$$

$$D_{iT} \frac{\partial^2 V_m(t, \mathbf{x})}{\partial y^2}\Big|_{i,j} \approx D_{iT}\Big[\frac{V_{i,j-1} - V_{i,j}}{\Delta y^2} + \frac{V_{i,j+1} - V_{i,j}}{\Delta y^2}\Big] \tag{3.47}$$

Using these results, (3.43) can be writen in a spatially discretized form as:

$$\frac{d\mathbf{v}}{dt} = -\mathbf{G_i}\mathbf{v} - \frac{1}{C_m}\mathbf{I_{ion}} + \mathbf{I_s} \tag{3.48}$$

$$\frac{d\mathbf{x_s}}{dt} = f(\mathbf{x_s}, \mathbf{v}) \tag{3.49}$$

Where the spatial derivatives are represented by means of the conductance matrix $\mathbf{G_i}$ as $\mathbf{G_i}.\mathbf{v} \approx -\nabla.(D_i \nabla V)$. The vectors $\mathbf{v}, \mathbf{I_{ion}}, \mathbf{x_s}, \mathbf{I_S}$ are of length $L = N_x \times N_y$ (the number of mesh points), the conductance matrix $\mathbf{G_i}$ is $L \times L$. $\mathbf{G_i}$ is sparse and pentadiagonal in the two-dimensional case. We used the Neumann no-flux boundary conditions (no current flows into or out of the external environment) [22].

Integration

To integrate (3.48), we used the semi-implicit method referred to in the electrophysiological literature as Crank-Nicholson method [26]. The linear term $\mathbf{G_i}.\mathbf{v}$ is treated implicitly as the weighted average (with weighting factor 1/2) of the spatial derivatives at the instants t and $t + 1$ like in the Crank-Nicholson method [26], the nonlinear term $\mathbf{I_{ion}}(\mathbf{x_s}, \mathbf{v})$, however, is treated explicitly. Hence

(3.48) becomes:

$$\frac{\mathbf{v^{t+1}} - \mathbf{v^t}}{\Delta t} = -\frac{1}{2}\mathbf{G_i}\Big[\mathbf{v^{t+1}} - \mathbf{v^t}\Big] - \frac{1}{C_m}\mathbf{I_{ion}} + \mathbf{I_s} \tag{3.50}$$

rearranging, we obtain:

$$\left[\frac{1}{2}\mathbf{G_i} + \frac{1}{\Delta t}\mathbf{I}\right]\mathbf{v^{t+1}} = -\left[\frac{1}{2}\mathbf{G_i} - \frac{1}{\Delta t}\mathbf{I}\right]\mathbf{v^t} - \frac{1}{C_m}\mathbf{I_{ion}} + \mathbf{I_s} \tag{3.51}$$

We see that this leads to a linear system of the form:

$$\mathbf{Ax} = \mathbf{b} \tag{3.52}$$

Where the matrix $\mathbf{A}$ is constant in time and thus assembled once before time iteration. However, the vector $\mathbf{b}$ depends on $\mathbf{v^t}$ and the ionic and stimulus currents, and therefore need to be update with time. Computing the solution at each time step involve:

1. Integrating the cellular ODEs at each node,
2. Assembling the vector $\mathbf{b}$,
3. Solving the linear system (3.52).

We used the conjugate gradients (CG) [51], a standard choice of iterative method for solving large sparse, symmetric, positive-definite problems.

Chapter 4

Effect of Cell Geometry on Conduction Velocity in a Sub-Cellular Model of Myocardium

We have studied the effect of cell geometry on propagation velocity of the cardiac impulse using a sub-cellular computer model of myocardium. Variation of cell size has only small effects on longitudinal and transverse conduction velocity, when the ratio of cell length/width is constant, for cell sizes (length, width) between ($60\mu m \times 20\mu m$) and ($120\mu m \times 40\mu m$) The results were not dependent on gap junction conductance (range $0.25\mu S - 1\mu S$), gap junction distribution or the specific tissue architecture. Longitudinal conduction velocity increased with the cell length/width ratio and transverse velocity decreased. The cell length/width ratio was a good estimator of the anisotropic ratio. In conclusion, cell length/width ratio is more important than cell size in determining conduction velocity.

4.1 Introduction

The velocity of propagation of the cardiac impulse is determined by structural factors including cell-to-cell gap junctional conductance, the resistance of the cytoplasm and the extracellular space as well as by membrane resistance and excitability [64].

Theoretical and experimental studies have shown that cell geometry also plays a role in determining conduction velocity [56]. In a single fiber, conduction velocity is approximately proportional to the square root of the fiber radius [56]. It is also well established that in multi-dimensional myocardium, conduction velocity of flat waves decreases with an increase in cell membrane surface/volume ratio [56]. Cardiomyocyte geometry varies among species [106], and for the same specie, it changes with development [112, 118]. Cell geometry could also be affected by disease [128].

A number of reports point to the importance of cell size on cardiac electrophysiology and have linked a larger cell size to an increase in conduction velocity. Experimentally, cell size is usually estimated from measurements of cell length and cell width [118, 128].

Spach et al [112] showed that propagation velocity is faster in cell cultures of adult canine cells than in cell cultures of neonatal cells, which are smaller in size and have larger input impedance. In their study, Spach et al [112] also found that cell size is more important in determining cell-to-cell conduction delays and the characteristics of the upstroke of the action potential than gap junction distribution.

In a study of impulse propagation in neonatal mouse synthetic strands, Thomas et al. [118] explained the slower conduction velocity measured in neonatal cell cultures when compared to adult mouse hearts by differences in cell length (the length of adult mouse myocytes is approximately twice the length of neonatal myocytes). They proposed that as cell length increases, the propagating impulse finds less gap junctions per unit length, and conduction velocity increases as a consequence of the decrease in effective axial resistance [118].

However, other studies are not consistent with the idea that a larger cell length and width should

result in faster conduction velocity. For example, despite major differences in cell length and width between 4-to-6 week old murine cardiomyocytes and adult canine cardiomyocytes [135, 134], in situ measurements of epicardial conduction velocities are within the same range of values [20, 46].

Ventricular hypertrophy following heart failure increases cell size. Recently published studies in hypertrophied hearts showed an increase in conduction velocity [128, 24, 121, 4]. One of those studies [128], using an experimental model of non-ischemic heart failure, linked an increase in conduction velocity with the larger cell length and width resulting from hypertrophy. However other studies with different experimental models of heart failure show no change [93, 138] or conduction velocity slowing [68, 3, 88, 2], despite hypertrophy.

Conflicting experimental evidence indicates that the effect of cell size on conduction velocity remains unclear. Our objective is to quantify the effect of cell length and width on propagation using a sub-cellular computer model of propagation that incorporates the naturally occurring discontinuities in myocardial tissue structure. Sub-cellular models were first developed by Spach et al. [110], and later used by other groups to study the effect of gap junction distribution [54] and gap junction remodeling [19] in cardiac tissue.

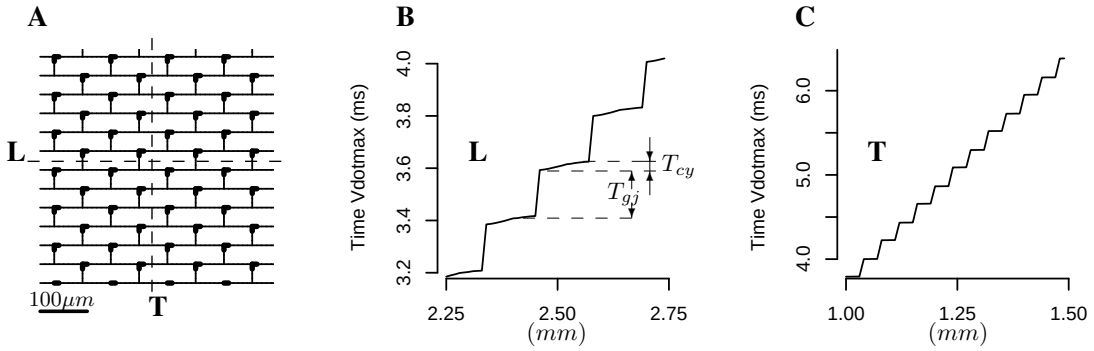

Figure 4.1: (A) Brick wall tissue structure consisting of cells 120μm in length and 40μm in width with 50% cell overlap. Gap junctions are located at the sites where the cell membrane is thicker (short bold black segments). (B) Activation times during propagation along a line parallel to the fiber orientation (dashed line labeled L in panel A). (C) Activation times during propagation along a line perpendicular to the fiber orientation (dashed line labeled T in panel A). Note the pattern of discontinuous conduction, as the cardiac impulse progresses through the cytoplasm and gap junctions connecting adjacent cells.

4.2 Methods

4.2.1 Numerical Methods

We performed all simulations in a 2D monodomain model with governing equation:

$\nabla \cdot ((1/(S_v R_i C_m))\nabla V_m) = (I_{ion}/C_m) + \partial V_m/\partial t,$

where V_m is the transmembrane potential (in mV), I_{ion} is the ionic current ($\mu A/cm^2$), R_i is the resistivity of the intracellular space, S_v is the surface to volume ratio ($2000cm^{-1}$) and C_m is the specific capacitance ($1\mu F/cm^2$). Neumann (non-flow) boundary conditions were used. Membrane dynamics (I_{ion}) were formulated by an ionic model of the action potential of normal canine epicardial cell (NZ cell dynamics) [18]. Cells were discretized with a space step of $10\mu m$ in both longitudinal and transverse directions. Each myocyte was electrically connected (only at the gap junctions) to neighboring myocytes. The basic tissue architecture used was a brick wall type of layout as shown in Fig. 5.1A. In some simulations, other tissue architectures were used, including layouts where cells had random lengths and widths, as shown in the Results below. Cell-to-cell gap junctional conductance (G_j) was $0.5\mu S$ for both side-to-side and end-to-end cell connections [135]. In some simulations, G_j values of $0.25\mu S$ and $1\mu S$ were also used. The resistivity of the cytoplasm was $150\Omega cm$. The governing equation was integrated using the semi-implicit Crank-Nicholson method

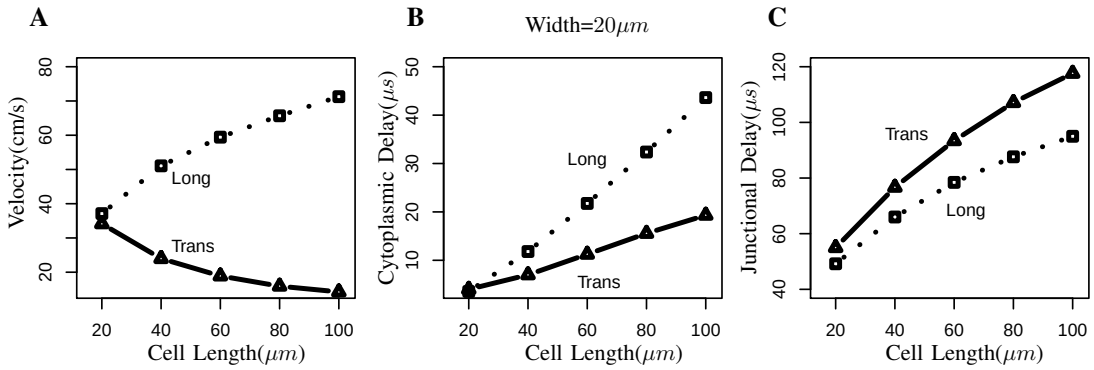

Figure 4.2: Longitudinal and transverse velocities for tissue structures with a fixed cell width ($20\mu m$) and varying cell length (panel A). Tissue structures are similar to the one shown in Fig. 5.1A. Corresponding cytoplasmic delay (B) and gap junction delay (C) during longitudinal (long) and transverse (trans) propagation.

with a time step of $1\mu s$.

4.2.2 Conduction Velocity and Anisotropy

We ran all simulations in preparations that had a size of 5 mm in the longitudinal direction and 2.5 mm in the direction transverse to the fiber orientation. Flat propagating wave fronts were initiated at the boundary of the preparation by an externally applied stimulus current (2x diastolic threshold). To avoid contamination by the electrical stimulus and the preparation boundaries, conduction velocity was calculated in the center of the preparation in an area of $500\mu m \times 500\mu m$. Velocity was calculated as the reciprocal of the regression coefficient of the activation times over space in the direction of propagation. The anisotropic ratio (ANR) was calculated as the ratio of the longitudinal (θ_L) and the transverse (θ_T) conduction velocities. A reduction of the spatial discretization step from $10\mu m$ to $5\mu m$ changed θ_L by $< 1\%$ and θ_T by $< 0.7\%$ for tissue structures with the narrowest cell width considered ($20\mu m$).

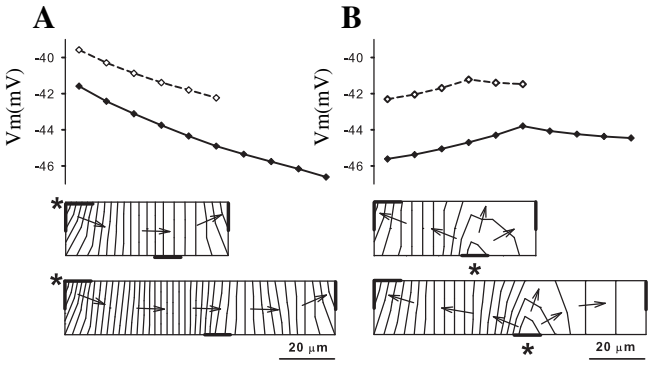

Figure 4.3: Top: Transmembrane potential (Vm) profile in a short ($60\mu m \times 20\mu m$, dashed) and a long cell ($100\mu m \times 20\mu m$ solid) at the time when the pre-junction node (asterisk) is activated, during longitudinal (A) and transverse (B) propagation. Bottom: Pattern of activation of the cytoplasm for a short and a long cell (isochrones every $1\mu s$) during longitudinal (A) and transverse (B) propagation. Arrows indicate the direction of propagation.

4.3 Results

4.3.1 Effect of Changing Cell Length on Conduction Velocity

Fig. 5.1 shows the tissue structure (Fig. 5.1A) and a plot of activation times during propagation in the longitudinal (Fig. 5.1B) and transverse (Fig. 5.1C) directions, across the center of the prepa-

ration (dashed lines in Fig. 5.1A), in a model with a brick wall structure with a 50% overlap. All cells were identical with length $120\mu m$ and width $40\mu m$. θ_L was $55.67cm/s$ and θ_T was $18.44cm/s$. Note the pattern of discontinuous propagation through the gap junctions and the cytoplasm.

Fig. 5.2A shows the effect of changing cell length on θ_L and θ_T, for a fixed cell width of $20\mu m$, in a tissue structure similar to the one shown in Fig. 5.1A. As cell length is increased, θ_L increases and θ_T decreases. The values of the corresponding cytoplasmic (T_{cy}) and junctional (T_{gj}) time delays during propagation are shown in Fig. 5.2B and 5.2C. During longitudinal propagation, T_{cy} increases approximately linearly with cell length. T_{gj} also increases with cell length, but the rate of increase diminishes with cell length. Despite the increase in T_{gj}, θ_L increases with cell length because for larger cell lengths, the propagating impulse encounters fewer junctions per unit length. During transverse propagation, both T_{cy} and T_{gj} increase with cell length, similarly to what occurred during longitudinal propagation. However, since cell width is fixed, a transversely propagating impulse encounters the same number of junctions per unit length regardless of cell length, and consequently θ_T decreases as cell length increases.

Fig. 5.3 (top) compares the Vm profile in a short (dashed line) and a long cell (solid line) at the time when the pre-junction node (asterisk) is activated, during longitudinal (Fig. 5.3A) and transverse (Fig. 5.3B) propagation. Less cell loading causes shorter cells to be more depolarized than

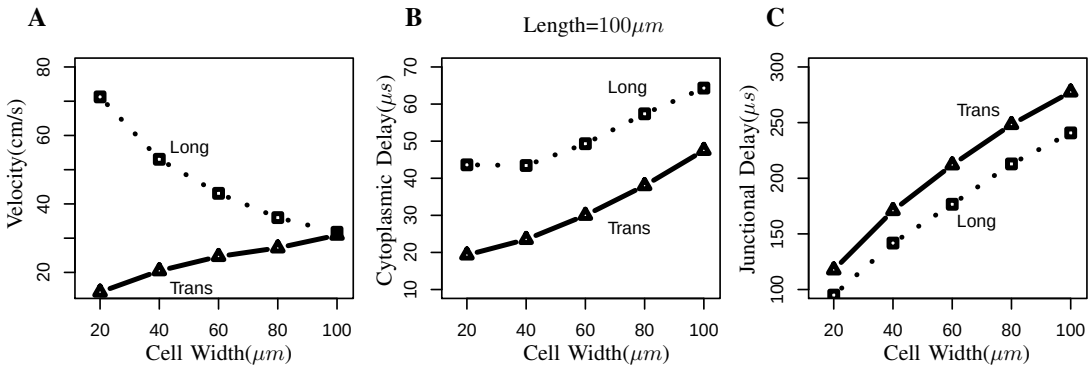

Figure 4.4: Longitudinal and transverse velocities for tissue structures with a fixed cell length ($100\mu m$) and varying cell width (panel A).Tissue structures are similar to the one shown in Fig. 5.1A. Corresponding cytoplasmic delay (B) and gap junction delay (C) during longitudinal (long) and transverse (trans) propagation.

longer cells, which results in a shorter T_{gj}. Isochronal maps show the activation of the cytoplasm in the longitudinal (Fig. 5.3A, bottom), and transversal (Fig. 5.3B, bottom) direction. The larger depolarization of shorter cells just before activation results in a faster conduction velocity in the cytoplasm. Also note that, during transverse propagation (Fig. 5.3B, bottom), as a consequence of less cell loading, propagation to the right (the cell end with one intercalated disk) is faster than propagation to the left (the cell end with two intercalated disks).

4.3.2 Effect of Changing Cell Width on Conduction Velocity

Fig. 5.4A shows the effect of changing cell width on θ_L and θ_T, for a fixed cell length of $100\mu m$, in a tissue structure similar to the one shown in Fig. 5.1A. As cell width is increased, θ_L decreases and θ_T increases. The corresponding T_{cy} and T_{gj} time delays during propagation are shown in Fig. 5.4B and 5.4C. During longitudinal propagation, both T_{cy} and T_{gj} increase with cell width. Since cell length is fixed, a longitudinally propagating impulse encounters the same number of junctions per unit length regardless of cell width, and consequently θ_L decreases as cell width increases. During transverse propagation, T_{cy} and T_{gj} also increase. However, despite that increase, θ_T increases with cell width because for larger cell widths, the propagating impulse encounters fewer junctions per unit length.

4.3.3 Effect of Cell Size on Propagation for Different Cell-to-Cell Gap Junction Conductance

To investigate the effect of cell size on propagation, we calculated θ_L and θ_T and ANR for two tissue structures consisting of cells with the same aspect ratio (cell length / cell width) but different cell size (Fig. 5.5). When $G_j = 0.5\mu S$, for the structure consisting of $60\mu m \times 20\mu m$ cells, θ_L was $59.44 cm/s$, and θ_T was $18.9 cm/s$. For the structure consisting of $120\mu m \times 40\mu m$ cells, θ_L was $55.67 cm/s$, and θ_T was $18.44 cm/s$. ANR was 3.14 and 3.02 respectively. The lack of a major effect of cell size on conduction velocity ($< 6\%$) can be understood from the results presented in Fig. 5.2 and 5.4. An increase in cell length results in an increase in θ_L and a decrease in θ_T, while

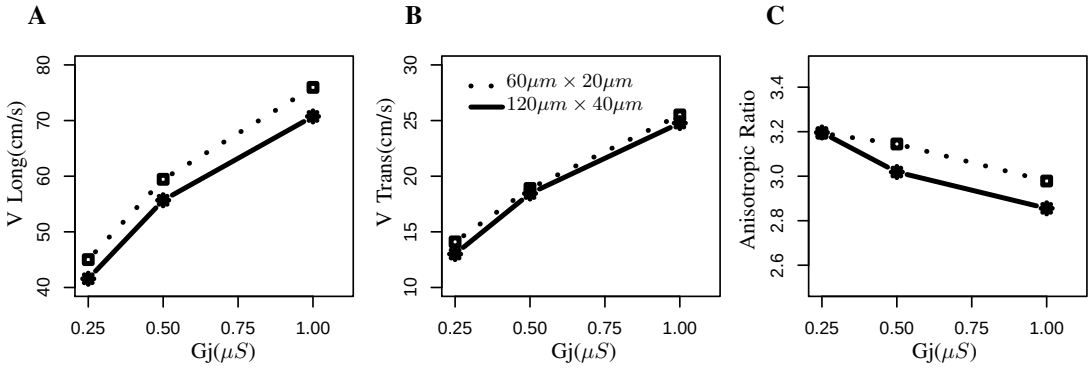

Figure 4.5: Longitudinal conduction velocity (A), transverse conduction velocity (B) and anisotropic ratio (C), for two tissue structures with cells of different size ($60\mu m \times 20\mu m$, dotted line; $120\mu m \times 40\mu m$, solid line),and different values of cell-to-cell conductance (G_j).

an increase in cell width results in a decrease in θ_L and an increase in θ_T. Therefore increasing both cell length and width tends to cancel their effects on θ_L and θ_T.

To investigate whether the (lack of) effect of cell size on conduction velocity was dependent on G_j we performed simulations with $G_j = 0.25\mu S$ and $G_j = 1\mu S$ (Fig. 5.5). For any given structure and cell size, θ_L and θ_T increase with G_j, while ANR decreases with G_j, consistent with earlier results [19]. But, the results show that the small effect of cell size on conduction velocity is not dependent on the value of G_j.

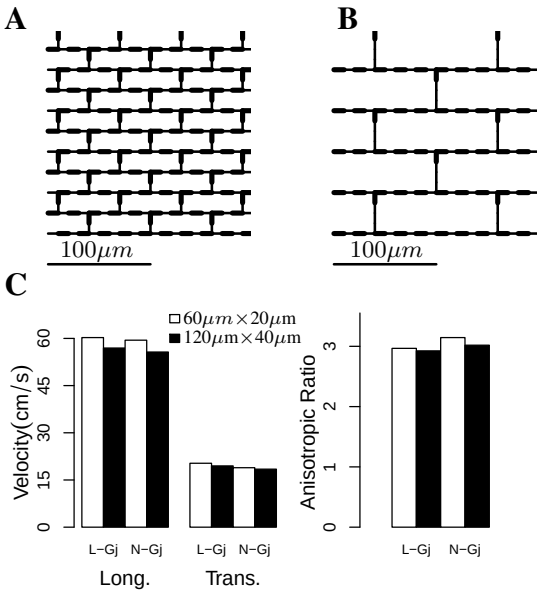

Figure 4.6: Tissue structures with lateralized gap junction distribution (L-Gj), for cell sizes $60\mu m \times 20\mu m$ (A) and $120\mu m \times 40\mu m$ (B). Gap junctions are located at the sites where the cell membrane is thicker (short bold black segments). (C) Longitudinal and transverse velocity, and anisotropy for the model with lateralized (L-Gj) and normal (N-Gj) gap junction distribution.

4.3.4 Effect of Cell Size on Propagation for Lateralized Gap Junction Distribution

In normal myocardium gap junctions are located within $10\% - 20\%$ of the cell ends at the intercalated disks (as it is shown in Fig. 5.1A). However, in neonatal cells [112] and during disease [20], gap junctions redistribute to the lateral membrane (i.e lateralize). When lateralized gap junctions form viable channels, θ_T increases as a result of a decrease in access resistance to the gap junction channels [19]. To test whether lateralized gap junctions modulate the effect of cell size on conduction velocity, we performed simulations with the layouts shown in Fig. 5.6A and 5.6B, and compared them to the layouts in Fig. 5.1A, for cell sizes $120\mu m \times 40\mu m$ and $60\mu m \times 20\mu m$ respectively. For each cell, the total number of G_j channels available (i.e. the total conductance, $0.5\mu S$) was distributed to the lateral membrane (L-Gj structure). Note that as a consequence of lateralization, each cell is electrically connected to six neighboring cells. For normal gap junction distribution (N-Gj, Fig. 5.1A), each cell is electrically connected to four neighboring cells. The values of θ_L, θ_T and ANR for N-Gj and L-Gj are shown in Fig. 5.6C. For the L-Gj structure, the difference in θ_L was 5.5% and the difference in θ_T was 4.2% (compared to differences in θ_L of 6.3% and in θ_T of 2.5% for the N-Gj structure). These results indicate that when gap junctions are distributed to the lateral membrane, conduction velocity is only marginally affected by cell size.

4.3.5 Effect of Cell Size on Propagation for Different Tissue Structures

The previous simulations were carried out in a tissue structure with a brick wall pattern with a 50% cell overlap (Fig. 5.1A). To investigate whether the effect of cell size on conduction velocity was dependent on the tissue structure, we calculated θ_L, θ_T and ANR for layouts with a brick wall pattern but with different cell overlap (33%, 83% and 100%) (Fig. 4.7A, 4.7B, 4.7C). Differences in conduction velocities for tissue structures containing cells with dimensions $60\mu m \times 20\mu m$ cells and tissue structures containing cells with dimensions $120\mu m \times 40\mu m$ are $< 10\%$. The results for all layouts were consistent with earlier results for a 50% overlap indicating that cell size does not have a major effect on conduction velocity or ANR.

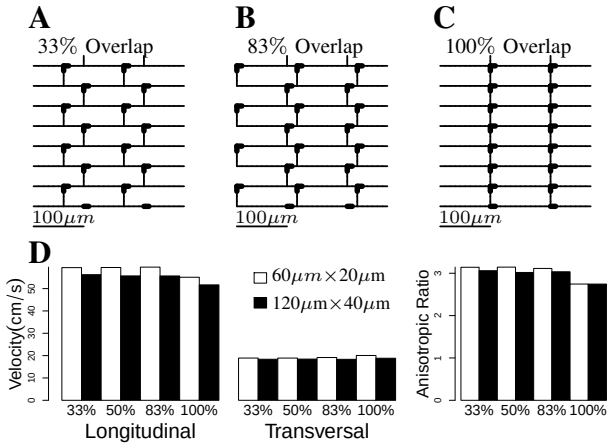

Figure 4.7: Tissue structures for 33% (A), 83% (B) and 100%(C) cell overlap with normal gap junction distribution. Gap junctions are located at the sites where the cell membrane is thicker (short bold black segments). (D) Longitudinal and transverse velocity, and anisotropy for the models with different % cell overlap.

4.3.6 Effect of Cell Size on Propagation in a Structure with Cells with Random Length and Width

In real myocardium there is variability in cell length and width. To investigate how variability in cell length and width affect the relationship between cell size and conduction velocity we performed the simulations shown in Fig. 4.8. In the layout with smaller cells, average cell length was 61 ± 14.7μm and average cell width 21.7 ± 5.9μm (Fig. 4.8A). In the layout with the larger cells, average cell length was 117.7 ± 18.8μm and average cell width 35.8 ± 8.7μm (Fig. 4.8B). Fig. 4.8C shows the calculated θ_L, θ_T and ANR in the random layout and in the brick wall with 50% overlap (shown here for comparison). Differences in conduction velocities for different cell sizes are < 10%. Therefore, similarly to what occurred in layouts with fixed cell length and width, in a random layout, cell size does not have a major effect on conduction velocity or ANR.

4.3.7 Effect of Cell Shape on Conduction Velocity

The results in Fig. 5.2A and 5.4A show that cell shape (ratio of cell length/width) have an effect on conduction velocity and ANR. The results in Fig. 5.2A and 5.4A are plotted in Fig. 4.9 to better illustrate the effect of cell shape on conduction velocity and ANR. As cell length/width increases, θ_L increases and θ_T decreases (Fig. 4.9A). Conduction velocities are proportional to tissue space constants, and the proportionality constant is a function of the active response of the cell

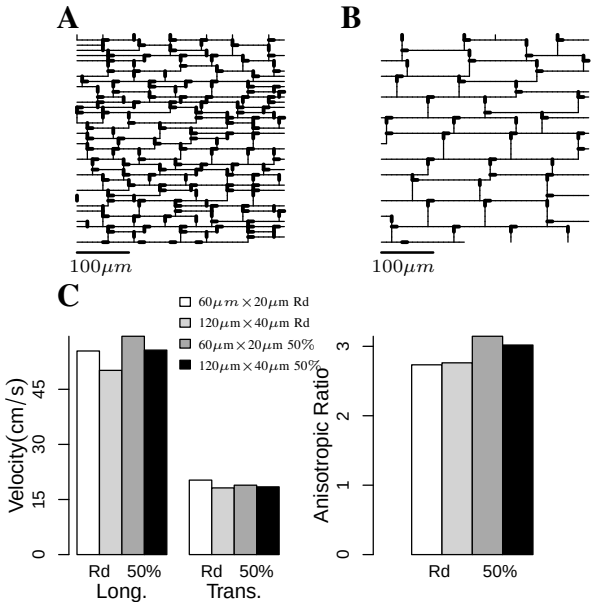

Figure 4.8: Tissue structures with cells with random lengths and widths with normal gap junction distribution for average cell sizes $\sim 60\mu m \times 20\mu m$ (A) and $\sim 120\mu m \times 40\mu m$ (B). Gap junctions are located at the sites where the cell membrane is thicker (short bold black segments). (C) Longitudinal and transverse velocity, and anisotropy for the model with random cell length and width (Rd) models and for the model with fixed cell length and width with 50% cell overlap (50%).

membrane (mostly sodium current). The dashed lines in Fig. 4.9A show θ_L and θ_T fitted to longitudinal (λ_L) and transverse (λ_T) space constants as $\theta_L = 900\lambda_L$ and $\theta_T = 900\lambda_T$. Expressions for λ_L and λ_T as a function of cell length/width and tissue parameters are shown in the Appendix (equation (4.4) and (4.5)). Fig. 4.9B shows ANR as a function of length/width ratio. Also shown in Fig. 4.9B (dashed line) is the λ_L/λ_T ratio (equation (4.6) in the Appendix). As cell-to-cell junctional resistance increases, $\lambda_L/\lambda_T \sim L/W$ in equation (4.6) (Appendix), and cell length/width ratio is a good approximation of ANR.

4.4 Discusion

In this paper we show that, for a given surface/volume ratio, cell shape (i.e. cell length / cell width) is more important in determining conduction velocity that cell size. Conduction velocities do not change significantly with an increase in cell length and width that keeps the length/width ratio constant. In the simulations presented here, conduction velocities in tissue structures with cell sizes (length x width) $60\mu m \times 20\mu m$ and $120\mu m \times 40\mu m$ differ by $< 6\%$ despite major differences in cell size (a factor of two). The results do not depend on cell-to-cell junctional conductance (Fig. 5.5) or on whether gap junctions are distributed along the cell membrane or are located at the end of

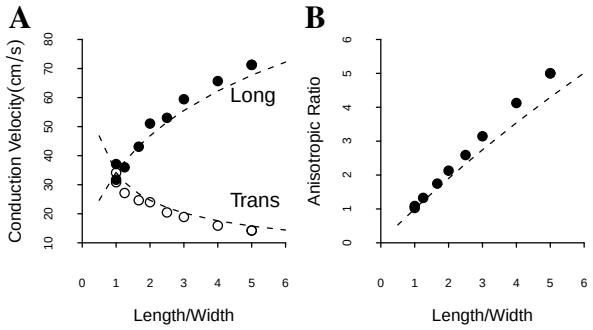

Figure 4.9: (A) Longitudinal (solid circles) and transverse(empty circles) velocity as a function of cell length/width ratio. Dashed lines in (A) plot velocities fitted to expressions of λ_L and λ_T derived in the Appendix (see text for explanation). (B) Anisotropic ratio as a function of cell length/width ratio. Dashed line in (B) plots the ratio λ_L/λ_T as a function of the cell length/width (equation (4.6) in Appendix).

the cells (Fig. 5.6). Furthermore, the results do not depend on cell layout. For random cell layouts, where average cell length and width differ by a factor of two, there are no major differences in conduction velocity or ANR (Fig. 4.8). On the other hand, cell shape is an important determinant of conduction velocity and ANR. As cell length/width increases θ_L increases and θ_T decreases (Fig. 4.9A). ANR is well approximated by cell length/width ratio especially as cell-to-cell conductance decreases (Fig. 4.9B and equation 6 in Appendix). Spach et al [112] showed that both θ_L and θ_T are faster in adult canine cell cultures than in neonatal canine cell cultures. The conduction velocities calculated in their computer models of neonatal and adult cells were in agreement with their experimental results. They attributed the larger conduction velocities measured (and simulated) to the larger size of adult myocytes. Even though average length and width of adult and neonatal myocytes is not given in the paper, we can estimate cell length/width ratio from the ANR: 2.94 for adult cell cultures and 2.75 for neonatal cell cultures [112]. Such a small change in ANR ($< 7\%$) is probably a consequence of a small change in cell length/width ratio. Therefore, according to our results, it is not likely that the observed differences in conduction velocity ($\sim 25\%$) are a consequence of changes in cell size or shape. Other factors like cell-to-cell conductance and cell surface/volume ratio, might have contributed to the observed differences in velocity. In their simulations, Spach et al [112] used a mean cell-to-cell conductance between neonatal cells ($0.63\mu S$) that is less than cell-to-cell conductance between adult cells ($0.77\mu S$) to reflect differences in Cx43 protein expression. A smaller cell-to-cell conductance between neonatal cells can explain the slower velocity of propagation in both longitudinal and transverse directions (Fig. 4) [19]. The larger surface/volume

ratio used in the neonatal model by Spach et al [112], results in smaller space constants (Appendix), and slower θ_L and θ_T in the neonatal model. Therefore, based on the simulations presented here, it is possible that the larger conduction velocity measured by Spach et al [112] in adult cell cultures (with respect to neonatal cell cultures) is not the result of differences in cell length and width but a consequence of differences in cell-to-cell conductance and surface/volume ratio (cell depth) between the two tissues.

Thomas et al. [118] explains the difference in θ_L between monolayers of neonatal murine cells and in intact adult mice hearts [46, 37] as a result of differences in cell size. In their measurements, both cell types have the same width ($\sim 15\mu m$), while the length of adult mice cells is approximately double the length of neonatal cells ($85\mu m$ vs. $42\mu m$). The results presented here are consistent with that explanation, because for a fixed cell width, an increase in cell length results in an increase in θ_L (Fig. 5.2). However, in the intact heart, the resistance of the restricted extracellular space is likely to influence θ_L [19]. While the larger cell length/width ratio is expected to result in an increase in θ_L (Fig. 4.9), the resistance of the extracellular space (which is negligible in monolayer cell cultures) is expected to decrease it [19].

Wiegerinck et al [128] attributed the increased conduction velocity ($\sim 18\%$) in an experimental model of rabbit heart failure to an $\sim 30\%$ increase of both cell length and width. According to our results, an increase in cell size that preserves the cell length/width ratio should not cause a major change in conduction velocity. Therefore our simulations cannot explain the link between cell size and conduction velocity proposed by Wiegerinck et al. [128]. Expression of Cx43 in hypertrophied hearts is about the same as control in epicardium and it is reduced in midmyocardium. It is unclear whether those changes in Cx43 would translate into a significant change in cell-to-cell conductance, and therefore contribute to the observed changes in conduction velocity. A possible explanation of the observed changes in conduction velocity is that, in addition to an increase in cell length and width, cell depth is also increased. In that case, the resulting decrease in surface-to-volume ratio with hypertrophy would result in an increase in space constant and conduction velocities (Appendix). To provide a link between changes in cell geometry and conduction velocity,

measurements of cell length and width might not be sufficient.

4.5 Conclusion

Cell geometry affects conduction velocity of the cardiac impulse. The most important geometrical factor in determining conduction velocity, for a given membrane surface/volume ratio, is cell length/width ratio. Tissue structures consisting of cells with different sizes but same cell length/width ratio have similar velocities. The results are not dependent on the specific tissue architecture. In conclusion, cell length/width ratio is more important than cell size in determining conduction velocity. This conclusion however does not imply that cell geometry is the only or the major factor determining conduction velocity. In addition to cell geometry several other factors, including Cx43 expression and phosphorylation state [3, 88, 2], the resistance of the extracellular space, membrane excitability, tissue geometry, and wave front curvature determine the velocity of a propagating wave [64].

4.6 Limitations

The simulations presented here are based on a computer model that is not directly derived from experimental data on tissue structure or gap junction location. While our results are not dependent on a specific tissue structure, or gap junction conductance and distribution, it is possible that incorporation of the natural variability in cell geometry, and a more realistic representation of the location of gap junctions in a computer model may lead to novel insights on the effect of cell geometry on propagation. Also, the model does not include an interstitial space [19, 111] or heterogeneities in membrane properties at the cell level, which are known to affect propagation [113, 67]. In future studies, we will investigate the effect of cell geometry in a computer model based on an experimentally derived tissue structure and gap junction distribution, following the methodology pioneered by Spach et al. [110].

4.7 Appendix

In myocardium, θ_L and θ_T are proportional to the corresponding longitudinal (λ_L) and transverse (λ_T) space constants. Here, we calculate the homogenized (continuous) λ_L and λ_T resulting from a discontinuous tissue structure consisting of cells with dimensions L (length), W (width) and h (depth), arranged with a 100% overlap (Fig. 4.7C). In the direction parallel to the fiber orientation (longitudinal), the resistance of a single cell can be expressed as:

$$R_{cell} = R_i(L/(Wh)) + R_g \tag{4.1}$$

where R_i is the resistivity of the intracellular space (Ωcm) and R_g is the junctional resistance (Ω) between two adjacent cells. The lumped intracellular resistance (resistance of the cytoplasm plus cell-to-cell junctional resistance) per unit length, r_i, in Ω/cm, can be expressed as:

$$r_i = R_{cell}/L \tag{4.2}$$

If R_m is the specific resistance of the membrane (Ωcm^2), the membrane resistance per unit length, r_m, in Ωcm, is:

$$r_m = R_m/(2W) \tag{4.3}$$

Since $\lambda_L = (r_m/r_i)^{0.5}$ and the membrane surface-to-volume ratio, S_v, can be expressed as (2/h), we obtain:

$$\lambda_L = (R_m/(S_v R_i + 2R_g(W/L)))^{0.5} \tag{4.4}$$

A similar analysis, assuming that the juntional resistance, R_g, is uniformly distributed through the lateral membrane, can be used to calculate the space constant in the direction transverse to the fibers, λ_T, which can be expressed as:

$$\lambda_T = (R_m/(S_v R_i + 2R_g(L/W)))^{0.5} \tag{4.5}$$

From (4.4) and (4.5), with $K = (2R_g)/(S_v R_i)$, we obtain:

$$(\lambda_L/\lambda_T) = ((1 + K(L/W))/(1 + K(W/L)))^{0.5} \tag{4.6}$$

We fitted the curves in 4.9A to equations (4.4) and (4.5) using $\theta_L = 900\lambda_L$ and $\theta_T = 900\lambda_T$ with parameters: $R_m = 6225\Omega cm^2$, $S_v = 2000cm^{-1}$, $R_i = 150\Omega cm$, and $R_g = 1/0.5\mu S = 2M\Omega$ (or $G_j = 0.5\mu S$)

Chapter 5

Unidirectional Block Caused by Heterogeneities in Cell Geometry and Gap Junction Conductance

We have studied the effect of heterogeneities in cell geometry (quantified as the ratio of cell length/width (L/W)) and gap junction conductance (G_j) on propagation and block of cardiac waves, using a sub-cellular computer model of myocardium. We found that, under conditions of reduced excitability, a wave propagating into a region with a larger cell L/W or into a region with higher G_j can result in propagation block. Since both, cell L/W and G_j are determinants of the space constant (λ), we quantified the conditions for conduction and block as a function of λ: block occurred when cardiac waves propagated into regions in which λ increased by $> 43\%$. Analysis of the rate of increase of λ with cell L/W and G_j indicate that tissue architectures with elongated cells (i.e. large cell L/W ratios) that are better coupled (i.e. large G_j) are less prone to block at sites of regional heterogeneities in cell geometry and/or cell coupling. Our findings could be useful to understand the mechanisms of block in cardiac pathologies that result in tissue architecture remodeling as well as to guide the design of artificial tissue architectures aimed at myocardium repair.

5.1 Introduction

Many clinically relevant cardiac arrhythmias have a reentrant mechanism, a pattern of excitation in which a wave rotates repeatedly around an anatomical or functional fulcrum [59]. Early on it was recognized that to initiate reentrant arrhythmias a region of unidirectional block must be established [64]. Regions of unidirectional block allow impulse propagation in one direction but block propagation in the opposite direction.

Unidirectional block can occur in homogeneous tissue [28, 95], in tissues with heterogeneities in cell properties (refractory period, membrane excitability) [43, 58] or in tissues with discontinuities in the macrostructure (muscle bundle branches, narrow isthmuses, pivot points, tissue expansions) [60, 114, 15, 16, 39]. The mechanism of formation of areas of unidirectional block in homogeneous tissue structures is related to the inherent functional heterogeneities created during propagation. For example unidirectional block can be created by electrical stimulation using cross-field stimulation protocol [41] or electrical stimulation in the tail of a propagating wave [95]. Heterogeneities in cell membrane properties, like refractory period and membrane excitability, result from spatial differences in the amount of remodeling of different ionic channels after the onset of heart failure, myocardial infarction or atrial fibrillation [80]. Discontinuities in the macrostructure can result from abnormal proliferation of connective tissue (fibrosis) that follows the process of aging and cardiac disease [31]. By separating the membranes of adjacent cells, fibrosis also causes a reduction in cell-to-cell electrical coupling with the consequent impairment in the propagation of the cardiac impulse [109].

In addition to discontinuities in the macrostructure, structural remodeling following heart disease can cause local heterogeneities in the tissue microstructure, like an increase in cell size (hypertrophy) [80] and remodeling of connexin43 (Cx43) [107], a protein channel that connects electrically the cytoplasm of adjacent cells. It has been shown that cell hypertrophy can affect propagation of cardiac action potentials resulting in an increase [128, 24, 121, 4] or decrease [3, 88, 2] in conduction velocity, but is not known if heterogeneities in cell size could result in propagation block,

and are responsible for initiation of arrhythmias in hypertrophied ventricles after heart failure. Myocardial infarction results in a reduction of the amount of Cx43 with the consequent decrease in gap junction conductance and conduction velocity [20]. Regions of heterogeneous Cx43 expression and gap junction conductance have been described in infarcted and failing hearts [88, 2, 20], but their impact on the development of unidirectional block and initiation of arrhythmias remains unclear.

Our objective is to quantify the conditions in which heterogeneities in the microstructure, specifically cell geometry and gap junction conductance, result in unidirectional block. We use sub-cellular computer models of propagation based on the model first developed by Spach et al. [110], which provides a realistic representation of the tissue microstructure including the natural variability in cell size and shape as well as the location of gap junctions. Sub-cellular models have also been used to investigate the effect of cell size and gap junction remodeling on propagation [54, 19, 120].

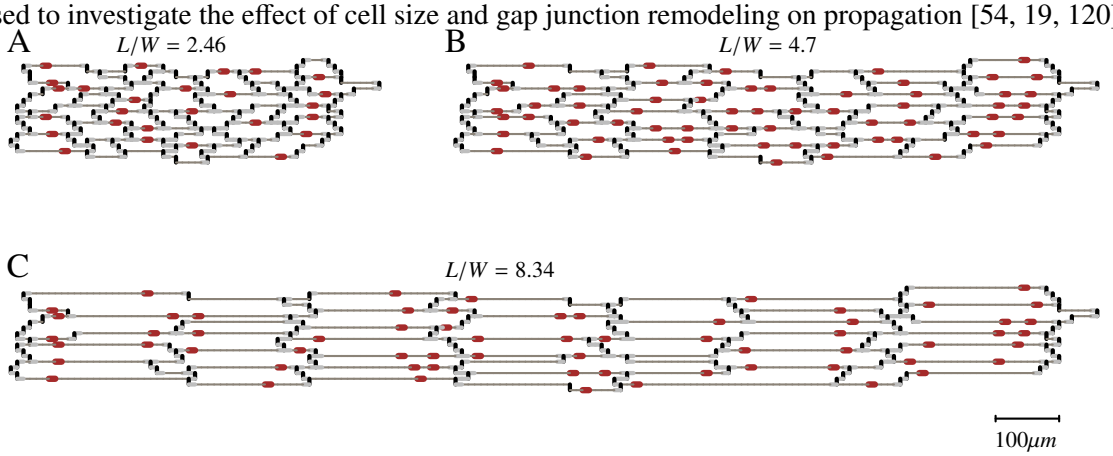

Figure 5.1: (B) Basic tissue architecture with natural variability in cell size and shape as well as the location of gap junctions, proposed by Spach et al. [110]. Average cell length/width is: $L/W = 4.7 \pm 1.33$. (A) Shortened version of the basic unit with average L/W of 2.46 ± 0.77. (C) Stretched version of the basic unit with $L/W = 8.34 \pm 2.47$. Cell width, gap junction location and cell-to-cell G_j were preserved in both (A) and (C) .

5.2 Methods

5.2.1 Numerical Methods

We performed all simulations in a 2D monodomain model with governing equation: $\nabla \cdot ((1/(S_v R_i C_m))\nabla V_m) = (I_{ion}/C_m) + \partial V_m/\partial t$, where V_m is the transmembrane potential (in mV), I_{ion} is the ionic current ($\mu A/cm^2$), R_i is the resistivity of the intracellular space, S_v is the surface to volume ratio ($2000cm^{-1}$) and C_m is the specific capacitance ($1\mu F/cm^2$). Neumann (non-flow) boundary conditions were used. Membrane dynamics (I_{ion}) were formulated by an ionic model of the action potential of normal canine epicardial cell (NZ cell dynamics) [18].

We used the tissue architecture proposed by Spach et al [110] (figure 5.1B) as the basis to create other architectures with different cell geometries or cell-to-cell gap junctional conductance (G_j). That tissue architecture is a realistic representation of the natural variability in cell size and shape as well as the location of gap junctions. Each myocyte was electrically connected to neighboring myocytes only at the gap junctions. To study the effect of heterogeneities in cell geometry on propagation, we created tissue architectures with different average cell length/width (L/W) ratios by shortening (figure 5.1A) or stretching (figure 5.1C) the basic tissue architecture (figure 5.1B) in the longitudinal direction (cell width, gap junction location and cell-to-cell G_j were preserved).

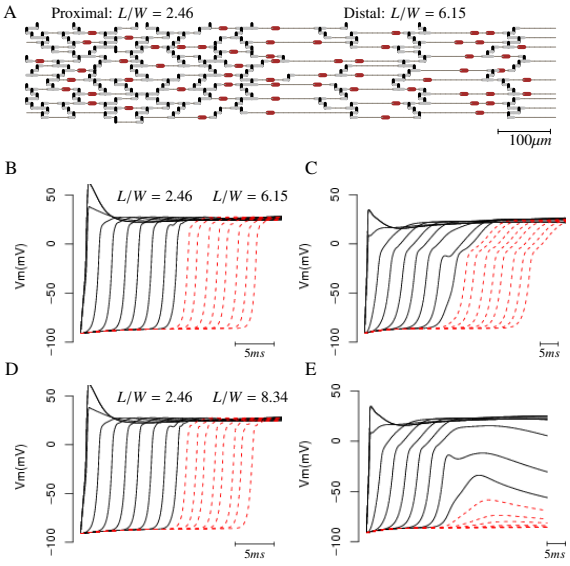

Figure 5.2: (A) Heterogeneous tissue structure with a proximal region with cell $L/W = 2.46 \pm 0.77$ and a distal region with cell $L/W = 6.15 \pm 1.75$. Cell-to-cell G_j was $0.41 \pm 0.2\mu S$ in both regions. Cardiac impulse initiated in the the proximal propagates to the distal for normal excitability (normal maximum sodium conductance) (B) or reduced excitability (30% normal maximum sodium conductance (C). When cell L/W in distal region is increased to 8.34 ± 2.47, AP propagates through the heterogeneity when excitability is normal (D) but block occurs with reduced excitability (E).

To study the effect of G_j heterogeneities on propagation, we used the tissue architecture proposed by Spach et al. [110] (figure 5.1B), with different regions having different cell-to-cell G_j while the location of gap junctions was preserved. The resistivity of the cytoplasm was $150\Omega cm$. Cells were discretized with a space step of $10\mu m$ in both longitudinal and transverse directions [120]. The governing equation was integrated using the semi-implicit Crank-Nicholson method with a time step of $1\mu s$.

5.2.2 Simulation Protocols

In a first set of simulations we studied propagation (and block) of the action potential at the boundary of a proximal and a distal region. Proximal and distal regions had either different cell geometry (cell L/W ratio) or different average cell-to-cell G_j. Flat propagating wave fronts were initiated at the boundary of the proximal or distal region of the preparation by an externally applied stimulus current (2x diastolic threshold). The size of the proximal and distal regions was about five space constants (λ).

In a second set of simulations we calculated λ for tissue architectures with different average cell L/W ratios and different cell-to-cell G_j. Longitudinal λ was calculated from the spatial decay of Vm in the direction of the fiber orientation, five membrane time constants ($40ms$) after one end of the preparation was clamped at $-65mV$.

5.3 Results

5.3.1 Propagation Block Caused by Heterogeneities in Cell Geometry

Figure 5.2 shows examples of propagation and block in preparations with heterogeneous cell geometry. Figure 5.2A shows a heterogeneous tissue structure with a proximal region with cell $L/W = 2.46 \pm 0.77$ and a distal region with cell $L/W = 6.15 \pm 1.75$. Cell-to-cell G_j was $0.41 \pm 0.2\mu S$ in both the proximal and the distal regions. When the cardiac impulse is initiated in the proximal region, the action potential propagates through the heterogeneity into the distal region both under

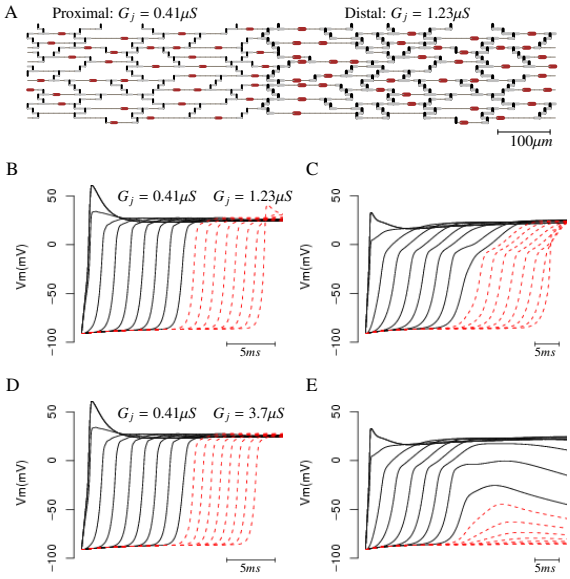

Figure 5.3: (A) Heterogeneous tissue structure with a proximal region with cell-to-cell Gap junction $G_j = 0.41 \pm 0.2\mu S$ and a distal region with $G_j = 1.23 \pm 0.59\mu S$. Cell L/W ratio was 2.46 ± 0.77 in both regions. Cardiac impulse initiated in the the proximal propagates to the distal for normal excitability (normal maximum sodium conductance) (B) or reduced excitability (30% normal maximum sodium conductance (C). When G_j in distal region is increased to $3.7 \pm 1.77\mu S$, AP propagates through the heterogeneity when excitability is normal (D) but block occurs with reduced excitability (E).

conditions of normal excitability (normal maximum sodium conductance, figure 5.2B) or reduced excitability (30% the normal value of maximum sodium conductance, figure 5.2C).

In contrast, when cell L/W ratio in the distal region is increased to 8.34 ± 2.47, the action potential propagates through the heterogeneity when excitability is normal (figure 5.2D) but block occurs with reduced excitability (figure 5.2E). Block is unidirectional because when the action potential propagates from the region with higher cell L/W ratio to the region of lower cell L/W ratio, block does not occur either for normal or reduced excitability (not shown). The results in figure 5.2

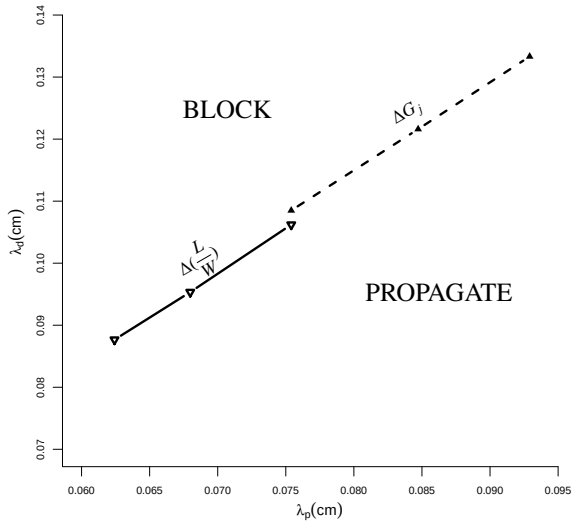

Figure 5.4: Propagation and block as a function of space constants in the proximal (λ_p) and the distal (λ_d), under conditions of reduced excitability. (Solid line): For preparations with heterogeneity in cell L/W ratio, block occurs when λ_d increases by $>\sim$ 40% over λ_p. (Dashed line): For preparations with heterogeneity in cell-to-cell G_j, block occurs when λ_d increases by $>\sim$ 43% over λ_p.

demonstrate that heterogeneities in cell L/W may lead to propagation block when the action potential propagates into a region of larger cell L/W ratio and excitability is reduced.

5.3.2 Propagation Block Caused by Heterogeneities in Gap Junctional Conductance

Figure 5.3 shows examples of propagation and block in preparations with the same cell geometry but heterogeneous cell-to-cell G_j. Figure 5.3A shows a preparation with a proximal region with $G_j = 0.41 \pm 0.2 \mu S$ and a distal region with $Gj = 3.7 \pm 1.77 \mu S$. Cell L/W ratio was 4.7 ± 1.33 for both the proximal and the distal regions. When the cardiac impulse is initiated in the proximal region, the action potential propagates through the heterogeneity into the distal region both under conditions of normal excitability (normal maximum sodium conductance, figure 5.3B) or reduced excitability (30% the normal value of maximum sodium conductance, figure 5.3C). In contrast, when G_j in the distal region is increased to $3.70 \pm 1.77 \mu S$, the action potential propagates through the heterogeneity during normal excitability (figure 5.3D) but blocks with reduced excitability (figure 5.3E). As in the case of heterogeneities in cell L/W, block is unidirectional because when the action potential propagates from the region with higher G_j to the region of lower G_j, block does not occur either for normal or reduced excitability (not shown). The results in figure 5.3 demonstrate that G_j heterogeneities may lead to propagation block when the action potential propagates into a region of higher cell-to-cell G_j and excitability is reduced.

5.3.3 Spatial Changes in Space Constant Causing Propagation Block

The results presented in figures 5.2 and 5.3 can be better understood in terms of the values of the space constants of the proximal (λ_p) and distal (λ_d) regions in the direction of the fiber orientation. We have shown in an earlier report [120] that cell L/W ratio and G_j are determinants of λ: a larger cell L/W ratio results in a larger λ; a larger cell-to-cell G_j results in a larger λ. Figure 5.4 summarizes the results of simulations resulting in propagation and block as a function of λ_p and λ_d under conditions of reduced excitability. For preparations with a heterogeneity in cell L/W ratio (figure 5.4, solid line), block occurs when a propagating wave enters a region in which λ increases

by at least $\sim$ 40%. For preparations with a heterogeneity in cell-to-cell G_j (figure 5.4, dashed line), block occurs when a propagating wave enters a region in which λ increases by at least $\sim$ 43%. Therefore, for the range of λ_p tested (0.062 - 0.095cm), regardless of the cellular determinant of a spatial heterogeneity in λ (geometry, cell-to-cell G_j), the action potential blocks when it propagates into a region in which λ increases > 43%.

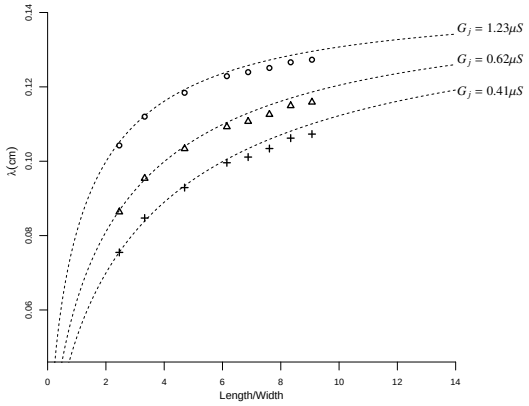

Figure 5.5: Relationship between λ and L/W. For a given G_j, λ increases with L/W; with a faster rate of increase for preparations with small L/W ratios. Variations in G_j modulates the relationship between λ and L/W; as G_j increases the curve between λ and L/W flattens.

5.3.4 Relationship of the Space Constant with Cell Length/Width ratio and Gap Junction Conductance

To further understand the conditions resulting in propagation and block in preparations with heterogeneities in cell geometry and G_j, we calculated λ, in the direction of the fiber orientation, for different preparations with different cell L/W ratios and G_j (figure 5.5). For a given value of cell-to-cell G_j, λ increases with cell L/W ratio (figure 5.5), which is consistent with our earlier results with

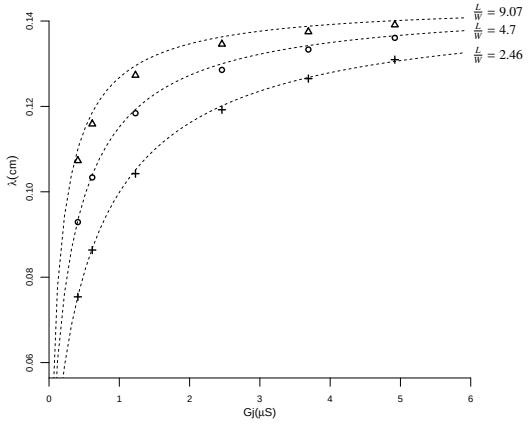

Figure 5.6: Relationship between λ and G_j. For a given L/W, λ increases with G_j; with a faster rate of increase for preparations with small G_j. Variations in L/W modulates the relationship between λ and G_j; as L/W increases the curve between λ and G_j flattens.

idealized tissue architectures [120]. Moreover, the rate of increase of λ with L/W is markedly faster for preparations with small L/W ratios than for preparations with large L/W ratios. This means that heterogeneities between regions with larger L/W ratios are less prone to block than heterogeneities between regions with smaller L/W ratios. For example, for $G_j = 0.41 \pm 0.2\mu S$ (figure 5.5), a heterogeneity between two regions with $L/W = 2.46$ and 8.34 causes block (figure 5.2) because the spatial difference in $\lambda(\Delta\lambda)$ is 41%, which is above the critical value for block (figure 5.4). On the other hand, a heterogeneity between two regions with $L/W = 3.3$ and 9.07 will not cause block because $\Delta\lambda = 27\%$, below the critical value for block (figure 5.4). As heterogeneous regions have larger L/W ratios, the less likely it is that the heterogeneity in cell geometry will cause block.

The effect of regional heterogeneities in cell geometry on propagation and block depends on cell-to-cell coupling. As cell-to-cell G_j increases the relationship between λ and the cell L/W ratio flattens (figure 5.5). For example, the increase in λ between preparations with $L/W = 2.46$ and 9.07, is 42% for $G_j = 0.41\mu S$, and decreases to 34% and 22% for $G_j = 0.62$ and $1.23\mu S$ respectively. While there is block at a heterogeneity between two regions with $L/W = 2.46$ and 9.07 when $G_j = 0.41\mu S$, there is no block at the same heterogeneity when G_j is increased to 0.62 or $1.23\mu S$.

Figure 5.6 shows the relationship between λ and cell-to-cell G_j for different cell L/W ratios. For a given value of cell L/W ratio, λ increases with G_j (figure 5.6), consistent with our earlier results relating G_j to conduction velocity [120]. The rate of increase of λ with G_j is markedly faster for preparations with small G_j than for preparations with large G_j. This means that, for a given L/W ratio, heterogeneities between regions with larger G_j are less prone to block than heterogeneities between regions with smaller G_j. For example, for $L/W = 2.46 \pm 0.77$ (figure 5.6), a heterogeneity between two regions with $G_j = 0.41$ and $1.48\mu S$ causes block because $\Delta\lambda$ is 44%, which is above the critical value for block (figure 5.4). On the hand, a heterogeneity between two regions with $Gj = 1.23$ and 4.92 does not cause block because $\Delta\lambda = 26\%$, below the critical value for block (figure 5.4). As heterogeneous regions have larger G_j, the less likely it is that the heterogeneity in cell-to-cell G_j will cause block.

The effect of regional heterogeneities in G_j on propagation and block depends on cell L/W ratio.

As cell L/W ratio increases the relationship between λ and G_j flattens (figure 5.6). For example, the increase in λ between preparations with $G_j = 0.41$ and 4.92, is 74% for $L/W = 2.46$, and decreases to 46% and 30% for $L/W = 4.7$ and 9.07 respectively. While there is block at a heterogeneity between two regions with $G_j = 0.41$ and $4.92\mu S$ when $L/W = 2.46$ or 4.7, there is no block at the same heterogeneity when L/W is increased to 9.07.

The results in figures 5.5 and 5.6 can be summarized as follows: as a consequence of the non-linear relationship between λ and cell L/W ratio and cell-to-cell G_j [120], preparations with more elongated cells (i.e. larger cell L/W ratios) and larger G_j are less prone to block at sites of regional heterogeneities in cell geometry and/or cell coupling.

5.4 Discusion

In this paper we show that heterogeneities in cell geometry and cell-to-cell conductance can result in block of propagating waves under conditions of reduced excitability. Block occurs when, as a result of changes in cell L/W and/or G_j, λ increases $> 43\%$ at a regional heterogeneity. Block does not occur when waves propagate in the direction of decreasing λ, and it is therefore unidirectional. We also found that different tissue architectures have different sensitivities to structural heterogeneities. Tissue architectures with more elongated cells (i.e. higher cell L/W) or with cells that are better coupled (i.e. G_j) are less prone to block than tissue architectures consisting of cells with lower L/W ratios and/or poorer coupling.

Patients with heart failure have hypertrophied ventricles and a high risk of developing cardiac arrhythmias [4]. Different types of remodeling occur during heart failure including an increase in cell size, ionic channel remodeling, reduced Cx43 expression and fibrosis [80]. It is likely that initiation of arrhythmias during heart failure is the result of a combination of one or more of those factors. In this study, we investigate if one of those factors, a change in cell geometry, could provide a substrate for initiation of arrhythmias. We found that in the absence of cell membrane heterogeneities or fibrosis, heterogeneities in average cell L/W could result in unidirectional block. There is evidence

of heterogeneous hypertrophy in clinical cases of hypertrophic cardiomyopathy [73], however, cell size in regions undergoing different levels of hypertrophy has not been quantified. Based on the simulations presented here we can make predictions that could be applicable to experimental and clinical situations involving hypertrophy. First, a regional increase in myocyte size without a change in myocyte L/W ratio does not result in block. This is consistent with our earlier findings showing that cell L/W is a better predictor of the effect of cell geometry on propagation and conduction velocity than cell size [120]. Second, the relative elongated shape of normal myocytes (cell L/W ratios between 4 and 6 [128, 3, 106]) is a safeguard against the effect of heterogeneities in cell geometry may have on creation of unidirectional block. Figure 5.5 shows that changes in cell L/W around average values of $L/W = 5$ will result in smaller changes in λ than the same changes around average values of L/W = 1. Unidirectional block is more likely to occur in tissue architectures with a small average cell L/W ratio (see below). Third, heterogeneities in cell geometry cannot be interpreted without taking into account the levels of Cx43 expression and gap junction conductance. figure 5.5 shows that a reduction in G_j results in a larger effect of existing heterogeneities in cell geometry. This is relevant to heart failure, because hypertrophy is accompanied by reduced expression of Cx43 and a consequent reduction in G_j [3, 88, 2].

One of the characteristics of hypertrophic cardiomyopathy is the disruption of the normal structure of myocardium causing cellular disorganization or disarray [73]. Cellular disarray is present in about 90% of patients with hypertrophic cardiomyopathy, and in about 5% of patients with other cardiac diseases [73]. In regions where cellular disarray occurs, adjacent myocytes can be aligned perpendicularly or obliquely to each other, instead of being aligned parallel to each other as in normal myocardium [74]. Cellular disarray is highly heterogeneous, and regions with severely disarray myocytes could be adjacent to regions of normally aligned myocytes [124]. Since disarrayed regions myocytes are distributed in all directions, it is expected that the regions with cellular disarray will have a small average cell L/W ratio. For example, in calculating the average cell L/W of a tissue structure with mycocyte disarray, myocytes (length l, width w) oriented perpendicularly to the direction of propagation, would be considered to have a length w and a width l. Figure 5.5 suggest

that boundaries between regions with severe cell disarray (cell L/W ratio $\sim$ 1-2) and regions with normal cell organization (cell L/W ratio $\sim$ 5) could form a substrate for unidirectional block and initiation of arrhythmias. Propagation is expected to block when a wave is propagating from the region with cellular disarray to the region with a normal cellular structure, because at the regional heterogeneity λ increases > 43% (figure 5.4).

The amount of Cx43 expression is reduced in heart failure [3, 88, 2] and after myocardial infarction [107, 20]. Remodeling of Cx43 could be heterogeneous, and could lead to initiation of arrhythmias [88, 20]. Our results suggest that boundaries between regions with different G_j (possibly as a result of different levels of Cx43 expression) provide a substrate for unidirectional block, a condition for initiation of arrhythmias (figure 5.3). Block occurs when a wave propagates from a region with poor coupling into a region with better coupling. The difference in G_j between the two regions has to be enough to produce a change in λ that is > 43%. Direct measurements of λ have been used to detect changes in levels of Cx43 expression [88, 37]. Therefore, it is possible to use similar techniques to detect regions with heterogeneous Cx43 expression. Alternatively, since conduction velocity is directly proportional to λ, measurements of conduction velocity by optical or electrical mapping can be used as a surrogate indicator of regions with heterogeneous G_j.

Heterogeneities in cell geometry and gap junction conductance result in unidirectional block under conditions of reduced excitability but not when membrane excitability is normal (figures 5.2 and 5.3). This is consistent with experimental demonstrations of block at macroscopic discontinuities in the tissue structure [114, 15, 16, 39]. Block occurred when membrane excitability was reduced as a consequence of an increase in extracellular potassium concentration [114], premature stimulation [114, 15, 16, 39], and reduced Na current due to disease or pharmacological interventions (Na current blockers) [16]. Here, membrane excitability was reduced by decreasing the maximum conductance of the Na channel, which simulates the decrease in Na current caused by disease [80] or pharmacological block. At muscle bundle branches and pivot points block occurs under different conditions that lead to a reduction of membrane excitability [114, 16]. Therefore, we expect that heterogeneities in cell geometry and G_j will also cause block when the reduction in membrane

excitability results from premature stimulation or elevation of extracellular potassium.

Stem cell-based therapy is an emerging therapeutic strategy for myocardial repair in patients with heart failure and myocardial infarction [14]. It has been shown that cell therapy could improve cardiac function and electrical viability in infarcted hearts, but after cell transplantation, arrhythmias still persist [77, 1, 98]. Heterogeneous distribution of stem cells in myocardium [77, 1] and the inability of transplanted cells to form gap junctions with cardiomyocytes have been related to arrhythmias [77, 1, 98]. Our results show that even if transplanted cells and cardiomyocytes form gap junctions, heterogeneities in cell geometry and G_j could lead to block and arrhythmogenesis. Furthermore, we show that structural block is less likely in heterogeneous tissue architectures consisting of well-coupled and elongated cells, a finding that could provide some guidance in the design and analysis of stem cell therapies.

5.5 Conclusion

Heterogeneities in cell geometry and gap junction conductance occurring during hypertrophic cardiomyopathy and myocardial infarction can provide a substrate for unidirectional block under conditions of reduced excitability. Block occurs when cardiac waves propagate into regions in which λ increases by $> 43\%$. Tissue architectures with elongated cells (i.e. large cell L/W ratios) that are better coupled (i.e. large G_j) are less prone to block at sites of regional heterogeneities in cell geometry and/or cell coupling.

5.6 Limitations

Following heart disease structural remodeling is extensive and is not limited to cell geometry and/or gap junction conductance. Ionic channel function is also remodeled [80], Cx43 may distribute to the lateral membrane [107] and fibrosis may occur [31]. In future studies we plan to incorporate those additional types of remodeling in our computer model, to investigate their role in the creation of arrhythmogenic substrates.

Chapter 6

Conclusions

The goal of this research was to investigate the effects of cell geometry and cell-to-cell gap-junctional conductance on the propagation of the cardiac action potential. The first part was to investigate whether cell shape, length/width ratio, is a better predictor for the velocity of the propagating wave than cell size (length and width). In the second part, our objective was to quantify the conditions in which heterogeneities in cell size and shape, as well as cell-to-cell gap-junctional conductance result in unidirectional block, a substrate for initiation of reentrant arrhythmias. This thesis demonstrates successful realization of the goals and paves the way for further investigations.

In the first part of this thesis, we developed two-dimensional microscopic models of cardiac myocardium tissue with theoretical cell structures. In these models, cells are conceived as rectangular shaped with given length and width. They are then laid out in a brick wall style with varying degree of overlap to obtain homogeneous tissue architectures. We used the monodomain approach described in chapter 3 to simulate action potential propagation within these theoretical subcellular myocardium.

We profiled the conduction velocity of the propagating wave with increasing cell length, while cell width was kept constant, to find that velocity increases in the longitudinal direction (θ_L)and decreases in the transverse direction (θ_T). In the other hand, for constant cell length, θ_L decreases while θ_T increases with increasing cell width. This results suggested that increasing both length

and width could cancel their effects on θ_L and θ_T. Indeed we found no major effect of cell size on velocity for tissue structures consisting of cells with the same aspect ratio(L/W), but different cell size. Therefore, cell shape (L/W) is a better predictor of velocity than cell size. We investigated and found that these results are not dependent on the conductance or distribution of the gap junctions as well as the specific tissue architecture used. We linked the cell length/width ratio to the tissue space constant, which is proportional to the conduction velocity, to find that length/width is a good approximation of anisotropic ratio (ANR=θ_L/θ_T); see chapter 4 appendix for the non-linear relationship between λ and cell L/W ratio and cell-to-cell G_j.

In the second part of the thesis, we used a basic tissue architecture with a realistic representation of the natural variability in cell size and shape as well as the location of gap junctions, as proposed by Spach et al [110]. To study the effect of heterogeneities in cell geometry on propagation, we modified this basic tissue to create other architectures with different cell geometries (by stretching or shortening) or cell-to-cell gap junctional conductance (G_j).

Simulations show that heterogeneities in cell L/W or G_j may lead to propagation block when the action potential propagates into a region of larger cell L/W ratio or higher cell-to-cell G_j and excitability is reduced. We then quantified the conditions for propagation and block as a function of λ, using the non-linear relationship between λ and cell L/W ratio and cell-to-cell G_j found earlier. Block occurred when cardiac waves propagated into regions in which λ increased by $> 43\%$. Furthermore, analysis of the rate of increase of λ with cell L/W and G_j indicate that different tissue architectures have different sensitivities to structural heterogeneities. Tissue architectures with elongated cells (i.e. large cell L/W ratios) that are better coupled (i.e. large G_j) are less prone to block at sites of regional heterogeneities in cell geometry and/or cell coupling.

6.1 Clinical implications

Our findings could be useful to understand pathological conditions involving remodeling. Different types of remodeling occur during heart failure including an increase in cell size, ionic channel

remodeling, reduced Cx43 expression and fibrosis [80]. Based on the simulations presented here on the effect of cell size, we can make predictions that could be applicable to experimental and clinical situations involving hypertrophy. There is evidence of heterogeneous hypertrophy in clinical cases of hypertrophic cardiomyopathy [73], however, cell size in regions undergoing different levels of hypertrophy has not been quantified. Based on the simulations presented here we can make predictions that could be applicable to experimental and clinical situations involving hypertrophy.

Remodeling of Cx43 could be heterogeneous, and could lead to initiation of arrhythmias [88, 20]. Our results suggest that boundaries between regions with different G_j (possibly as a result of different levels of Cx43 expression) provide a substrate for unidirectional block, a condition for initiation of arrhythmias. Direct measurements of λ have been used to detect changes in levels of Cx43 expression [88, 37]. Therefore, it is possible to use similar techniques to detect regions with heterogeneous Cx43 expression. Alternatively, since conduction velocity is directly proportional to λ, measurements of conduction velocity by optical or electrical mapping can be used as a surrogate indicator of regions with heterogeneous G_j.

Our findings could also be used to guide the design of artificial tissue architectures aimed at myocardium repair. Stem cell-based therapy is an emerging therapeutic strategy for myocardial repair in patients with heart failure and myocardial infarction [14]. Heterogeneous distribution of stem cells in myocardium [77, 1] and the inability of transplanted cells to form gap junctions with cardiomyocytes have been related to arrhythmias [77, 1, 98]. Our results show that even if transplanted cells and cardiomyocytes form gap junctions, heterogeneities in cell geometry and G_j could lead to block and arrhythmogenesis. Furthermore, we show that structural block is less likely in heterogeneous tissue architectures consisting of well-coupled and elongated cells, a finding that could provide some guidance in the design and analysis of stem cell therapies.

6.2 Model Shortcomings and Future Studies

Heart disease structural remodeling is not limited to cell geometry and/or gap junction conductance. Ionic channel function is also remodeled [80], Cx43 may distribute to the lateral membrane [107] and fibrosis may occur [31]. Our model looked at the isolated effect of cell geometry and/or gap junction modeling. In future studies we plan to incorporate those additional types of remodeling in our computer model, to investigate their role in the creation of arrhythmogenic substrates as well as possible effects on the velocity of the propagating wave.

Also, the model does not include an interstitial space [19, 111] which is known to affect propagation. In future studies, we will expand our models to incorporate the interstitial space and use the more complex bidomain numerical techniques to solve the corresponding PDEs.

Cardiac myocytes coexist with nonmyocytes; notably fibroblasts [17]. It has been well established that the presence of fibroblasts in myocardium affects propagation of the cardiac impulse and is a cause of arrhythmogenesis [109, 123, 133]. In future studies, we plan to incorporate the coupling of fibroblasts with myocytes within our model.

One of the characteristics of hypertrophic cardiomyopathy is the disruption of the normal structure of myocardium causing cellular disorganization or disarray [73]. In regions where cellular disarray occurs, adjacent myocytes can be aligned perpendicularly or obliquely to each other, instead of being aligned parallel to each other as in normal myocardium [74]. Cellular disarray is highly heterogeneous, and regions with severely disarray myocytes could be adjacent to regions of normally aligned myocytes [124]. Our results suggest that boundaries between regions with severe cell disarray and regions with normal cell organization could form a substrate for unidirectional block and initiation of arrhythmias. In future work, we will develop a model architecture incorporating cellular disarray in order to verify these assumptions.

In future efforts, we will also attempt the use of experimentally derived tissue structure and gap junction distribution. We will use immunofluorescent confocal imaging to label the cell membrane outlines as well as the gap junction locations to obtain cell geometry and interconnections. An

improvement over the technique used by Spach et al. [110] (and reproduced in the second part of this thesis), where cells were isolated in culture to extract their dimensions before fitting them together to form a group of cell.

Bibliography

[1] M. Roselle Abraham, Charles A Henrikson, Leslie Tung, Marvin G Chang, Miguel Aon, Tian Xue, Ronald A Li, Brian O' Rourke, and Eduardo Marbn. Antiarrhythmic engineering of skeletal myoblasts for cardiac transplantation. *Circ Res*, 97(2):159–167, Jul 2005.

[2] Fadi G Akar, Robert D Nass, Samuel Hahn, Eugenio Cingolani, Manish Shah, Geoffrey G Hesketh, Deborah DiSilvestre, Richard S Tunin, David A Kass, and Gordon F Tomaselli. Dynamic changes in conduction velocity and gap junction properties during development of pacing-induced heart failure. *Am J Physiol Heart Circ Physiol*, 293(2):H1223–H1230, Aug 2007.

[3] Fadi G Akar, David D Spragg, Richard S Tunin, David A Kass, and Gordon F Tomaselli. Mechanisms underlying conduction slowing and arrhythmogenesis in nonischemic dilated cardiomyopathy. *Circ Res*, 95(7):717–725, Oct 2004.

[4] K. P. Anderson, R. Walker, P. Urie, P. R. Ershler, R. L. Lux, and S. V. Karwandee. Myocardial electrical propagation in patients with idiopathic dilated cardiomyopathy. *J Clin Invest*, 92(1):122–140, Jul 1993.

[5] C. Antzelevitch, W. Shimizu, G. X. Yan, S. Sicouri, J. Weissenburger, V. V. Nesterenko, A. Burashnikov, J. Di Diego, J. Saffitz, and G. P. Thomas. The M cell: its contribution to the ECG and to normal and abnormal electrical function of the heart. *J Cardiovasc Electrophysiol*, 10(8):1124–1152, Aug 1999.

[6] Travis M Austin, Darren A Hooks, Peter J Hunter, David P Nickerson, Andrew J Pullan, Gregory B Sands, Bruce H Smaill, and Mark L Trew. Modeling cardiac electrical activity at the cell and tissue levels. *Ann N Y Acad Sci*, 1080:334–347, Oct 2006.

[7] J. W. Bassani, R. A. Bassani, and D. M. Bers. Relaxation in rabbit and rat cardiac cells: species-dependent differences in cellular mechanisms. *J Physiol*, 476(2):279–293, Apr 1994.

[8] G. W. Beeler and H. Reuter. Reconstruction of the action potential of ventricular myocardial fibres. *J Physiol*, 268(1):177–210, Jun 1977.

[9] Robert M. Berne. *Physiology*. C.V Mosby, 2004.

[10] Robert M. Berne and Matthew N. Levy. *Cardiovascular physiology*. St. Louis, MO : Mosby, 2001.

[11] J. Billette. Atrioventricular nodal activation during periodic premature stimulation of the atrium. *Am J Physiol*, 252(1 Pt 2):H163–H177, Jan 1987.

[12] J. Billette, M. J. Janse, F. J. van Capelle, R. H. Anderson, P. Touboul, and D. Durrer. Cycle-length-dependent properties of AV nodal activation in rabbit hearts. *Am J Physiol*, 231(4):1129–1139, Oct 1976.

[13] Martin Buist, Gregory Sands, Peter Hunter, and Andrew Pullan. A deformable finite element derived finite difference method for cardiac activation problems. *Ann Biomed Eng*, 31(5):577–588, May 2003.

[14] Nenad Bursac, Robert D Kirkton, Luke C McSpadden, and Brian Liau. Characterizing functional stem cell-cardiomyocyte interactions. *Regen Med*, 5(1):87–105, Jan 2010.

[15] C. Cabo, A. M. Pertsov, W. T. Baxter, J. M. Davidenko, R. A. Gray, and J. Jalife. Wavefront curvature as a cause of slow conduction and block in isolated cardiac muscle. *Circ Res*, 75(6):1014–1028, Dec 1994.

[16] C. Cabo, A. M. Pertsov, J. M. Davidenko, W. T. Baxter, R. A. Gray, and J. Jalife. Vortex shedding as a precursor of turbulent electrical activity in cardiac muscle. *Biophys J*, 70(3):1105–1111, Mar 1996.

[17] Candido Cabo. Modulation of impulse propagation by fibroblasts. *Am J Physiol Heart Circ Physiol*, 294(5):H1992–H1993, May 2008.

[18] Candido Cabo and Penelope A Boyden. Electrical remodeling of the epicardial border zone in the canine infarcted heart: a computational analysis. *Am J Physiol Heart Circ Physiol*, 284(1):H372–H384, Jan 2003.

[19] Candido Cabo and Penelope A Boyden. Extracellular space attenuates the effect of gap junctional remodeling on wave propagation: a computational study. *Biophys J*, 96(8):3092–3101, Apr 2009.

[20] Candido Cabo, Jianan Yao, Penelope A Boyden, Shan Chen, Wajid Hussain, Heather S Duffy, Edward J Ciaccio, Nicholas S Peters, and Andrew L Wit. Heterogeneous gap junction remodeling in reentrant circuits in the epicardial border zone of the healing canine infarct. *Cardiovasc Res*, Jul 2006.

[21] R. A. Chapman and C. H. Fry. An analysis of the cable properties of frog ventricular myocardium. *J Physiol*, 283:263–282, Oct 1978.

[22] R. H. Clayton and A. V. Panfilov. A guide to modelling cardiac electrical activity in anatomically detailed ventricles. *Prog Biophys Mol Biol*, 96(1-3):19–43, 2008.

[23] L. Clerc. Directional differences of impulse spread in trabecular muscle from mammalian heart. *J Physiol*, 255(2):335–346, Feb 1976.

[24] M. Cooklin, W. R. J. Wallis, D. J. Sheridan, and C. H. Fry. Conduction velocity and gap junction resistance in hypertrophied, hypoxic guinea-pig left ventricular myocardium. *Exp Physiol*, 83(6):763–770, 1998.

[25] M. Courtemanche, R. J. Ramirez, and S. Nattel. Ionic mechanisms underlying human atrial action potential properties: insights from a mathematical model. *Am J Physiol*, 275(1 Pt 2):H301–H321, Jul 1998.

[26] Nicolson P. Crank, J. A practical method for numerical evaluation of solutions of partial differential equations of the heat conduction type. *Proc. Camb. Phil. Soc.*, 1947.

[27] Howard J. Curtis and Kenneth S. Cole. Transverse electric impedance of the squid giant axon. *J. Gen. Physiol.*, 21(6):757–765, July 1938.

[28] J M Wharton A S Tang W M Smith D W Frazier, P D Wolf and R E Ideker. Stimulus induced critical point. mechanism for electrical initiation of reentry in normal canine myocardium. *J Clin Invest.*, 83(3):1039:1052., 1989 March.

[29] J. M. de Bakker, R. Coronel, S. Tasseron, A. A. Wilde, T. Opthof, M. J. Janse, F. J. van Capelle, A. E. Becker, and G. Jambroes. Ventricular tachycardia in the infarcted, Langendorff-perfused human heart: role of the arrangement of surviving cardiac fibers. *J Am Coll Cardiol*, 15(7):1594–1607, Jun 1990.

[30] J. M. de Bakker, F. J. van Capelle, M. J. Janse, S. Tasseron, J. T. Vermeulen, N. de Jonge, and J. R. Lahpor. Slow conduction in the infarcted human heart. 'Zigzag' course of activation. *Circulation*, 88(3):915–926, Sep 1993.

[31] Sanne de Jong, Toon Ab van Veen, Harold Vm van Rijen, and Jacques Mt de Bakker. Fibrosis and cardiac arrhythmias. *J Cardiovasc Pharmacol*, Dec 2010.

[32] S. S. Demir, J. W. Clark, C. R. Murphey, and W. R. Giles. A mathematical model of a rabbit sinoatrial node cell. *Am J Physiol*, 266(3 Pt 1):C832–C852, Mar 1994.

[33] Sanda Despa, Mohammed A Islam, Steven M Pogwizd, and Donald M Bers. Intracellular [Na+] and Na+ pump rate in rat and rabbit ventricular myocytes. *J Physiol*, 539(Pt 1):133–143, Feb 2002.

[34] Stefan Dhein. *Cardiac gap junctions : physiology, regulation, pathophysiology, and pharmacology*. Basel ; New York : Karger, 1998.

[35] P. J. Diaz, Y. Rudy, and R. Plonsey. Intercalated discs as a cause for discontinuous propagation in cardiac muscle: a theoretical simulation. *Ann Biomed Eng*, 11(3-4):177–189, 1983.

[36] D. DiFrancesco and D. Noble. A model of cardiac electrical activity incorporating ionic pumps and concentration changes. *Philos Trans R Soc Lond B Biol Sci*, 307(1133):353–398, Jan 1985.

[37] B. C. Eloff, D. L. Lerner, K. A. Yamada, R. B. Schuessler, J. E. Saffitz, and D. S. Rosenbaum. High resolution optical mapping reveals conduction slowing in connexin43 deficient mice. *Cardiovasc Res*, 51(4):681–690, 2001.

[38] A. Fabiato and F. Fabiato. Contractions induced by a calcium-triggered release of calcium from the sarcoplasmic reticulum of single skinned cardiac cells. *J Physiol*, 249(3):469–495, Aug 1975.

[39] V. G. Fast and A. G. Klber. Cardiac tissue geometry as a determinant of unidirectional conduction block: assessment of microscopic excitation spread by optical mapping in patterned cell cultures and in a computer model. *Cardiovasc Res*, 29(5):697–707, May 1995.

[40] J. FLEISCHHAUER, L. LEHMANN, and A. G. KLEBER. Electrical resistances of interstitial and microvascular space as determinants of the extracellular electrical-field and velocity of propagation in ventricular myocardium. *CIRCULATION*, 92(3):587–594, 1995.

[41] D. W. Frazier, P. D. Wolf, J. M. Wharton, A. S. Tang, W. M. Smith, and R. E. Ideker. Stimulus-induced critical point. mechanism for electrical initiation of reentry in normal canine myocardium. *J Clin Invest*, 83(3):1039–1052, Mar 1989.

[42] Plank Genot. Using monodomain computer models for the simulation of electric fields during excitation spread in cardiac tissue. In *Biomathematics: Modelling and Simulation,*. World Scientific Publishing Company; 1 edition, 2006.

[43] W. B. Gough, R. Mehra, M. Restivo, R. H. Zeiler, and N. el Sherif. Reentrant ventricular arrhythmias in the late myocardial infarction period in the dog. 13. correlation of activation and refractory maps. *Circ Res*, 57(3):432–442, Sep 1985.

[44] Henry Gray. *Anatomy of the human body*. Philadelphia: Lea & Febiger, 2000.

[45] J. L. Greenstein, R. Wu, S. Po, G. F. Tomaselli, and R. L. Winslow. Role of the calcium-independent transient outward current I(to1) in shaping action potential morphology and duration. *Circ Res*, 87(11):1026–1033, Nov 2000.

[46] D. E. Gutstein, G. E. Morley, H. Tamaddon, D. Vaidya, M. D. Schneider, J. Chen, K. R. Chien, H. Stuhlmann, and G. I. Fishman. Conduction slowing and sudden arrhythmic death in mice with cardiac-restricted inactivation of connexin43. *Circ Res*, 88(3):333–339, 2001.

[47] D. M. Harrild, R. C. Penland, and C. S. Henriquez. A flexible method for simulating cardiac conduction in three-dimensional complex geometries. *J Electrocardiol*, 33(3):241–251, Jul 2000.

[48] A.A. Henriquez, C.S. Papazoglou. Using computer models to understand the roles of tissue structure and membrane dynamics in arrhythmogenesis. In *Proceedings of the IEEE*, 1996.

[49] C. S. Henriquez and R. Plonsey. Effect of resistive discontinuities on waveshape and velocity in a single cardiac fibre. *Med Biol Eng Comput*, 25(4):428–438, Jul 1987.

[50] Craig S. Henriquez and Joseph V. Tranquillo. *Quantitative Cardiac Electrophysiology*, chapter Modeling the Impact of Cardiac Tissue Structure on Current Flow and Wavefront Propagation, pages 105–137. New York: Marcel Dekker, 2002.

[51] Eduard Hestenes, Magnus R.; Stiefel. Methods of conjugate gradients for solving linear systems. *Journal of Research of the National Bureau of Standards*, 1952.

[52] A. L. HODGKIN and A. F. HUXLEY. A Qantitative description of membrane current and its application to conduction and excitation in nerve. *J Physiol*, 117(4):500–544, Apr 1952.

[53] R. H. Hoyt, M. L. Cohen, and J. E. Saffitz. Distribution and three-dimensional structure of intercellular junctions in canine myocardium. *Circ Res*, 64(3):563–574, Mar 1989.

[54] Marjorie Letitia Hubbard, Wenjun Ying, and Craig S Henriquez. Effect of gap junction distribution on impulse propagation in a monolayer of myocytes: a model study. *Europace*, 9 Suppl 6:vi20–vi28, Nov 2007.

[55] P. Hunter, P. Robbins, and D. Noble. The iups human physiome project. *PFLUGERS ARCHIV-EUROPEAN JOURNAL OF PHYSIOLOGY*, 445(1):1–9, 2002.

[56] J.J.B. Jack, D. Noble, and R.W Tsien. *Electric current flow in excitable cells*. Oxford University Press, 1983.

[57] James Sneyd James Keener. *Mathematical Physiology*. Springer; 1 edition, 2001.

[58] M. J. Janse and A. G. Klber. Electrophysiological changes and ventricular arrhythmias in the early phase of regional myocardial ischemia. *Circ Res*, 49(5):1069–1081, Nov 1981.

[59] M. J. Janse and A. L. Wit. Electrophysiological mechanisms of ventricular arrhythmias resulting from myocardial ischemia and infarction. *Physiol Rev*, 69(4):1049–1169, Oct 1989.

[60] R. W. Joyner. Mechanisms of unidirectional block in cardiac tissues. *Biophys J*, 35(1):113–125, Jul 1981.

[61] S. Kanno and J. E. Saffitz. The role of myocardial gap junctions in electrical conduction and arrhythmogenesis. *Cardiovasc Pathol*, 10(4):169–177, 2001.

[62] J. P. Keener and K. Bogar. A numerical method for the solution of the bidomain equations in cardiac tissue. *Chaos*, 8(1):234–241, Mar 1998.

[63] Richard E. Klabunde. *Cardiovascular physiology concepts*. Philadelphia : Lippincott Williams & Wilkins, 2005.

[64] Andre G Kleber and Yoram Rudy. Basic mechanisms of cardiac impulse propagation and associated arrhythmias. *Physiol Rev*, 84(2):431–488, Apr 2004.

[65] James Kneller, Rafael J Ramirez, Denis Chartier, Marc Courtemanche, and Stanley Nattel. Time-dependent transients in an ionically based mathematical model of the canine atrial action potential. *Am J Physiol Heart Circ Physiol*, 282(4):H1437–H1451, Apr 2002.

[66] I. Kodama, A. Wilde, M. J. Janse, D. Durrer, and K. Yamada. Combined effects of hypoxia, hyperkalemia and acidosis on membrane action potential and excitability of guinea-pig ventricular muscle. *J Mol Cell Cardiol*, 16(3):247–259, Mar 1984.

[67] Jan P Kucera, Stephan Rohr, and Yoram Rudy. Localization of sodium channels in intercalated disks modulates cardiac conduction. *Circ Res*, 91(12):1176–1182, Dec 2002.

[68] Kenneth R Laurita, Emil Thomas Chuck, Tianen Yang, Wei-Qiang Dong, Yuri A Kuryshev, Gary M Brittenham, David S Rosenbaum, and Arthur M Brown. Optical mapping reveals conduction slowing and impulse block in iron-overload cardiomyopathy. *J Lab Clin Med*, 142(2):83–89, Aug 2003.

[69] W. M. Lue and P. A. Boyden. Abnormal electrical properties of myocytes from chronically infarcted canine heart. Alterations in Vmax and the transient outward current. *Circulation*, 85(3):1175–1188, Mar 1992.

[70] C. H. Luo and Y. Rudy. A model of the ventricular cardiac action potential. Depolarization, repolarization, and their interaction. *Circ Res*, 68(6):1501–1526, Jun 1991.

[71] C. H. Luo and Y. Rudy. A dynamic model of the cardiac ventricular action potential. I. Simulations of ionic currents and concentration changes. *Circ Res*, 74(6):1071–1096, Jun 1994.

[72] C. H. Luo and Y. Rudy. A dynamic model of the cardiac ventricular action potential. II. Afterdepolarizations, triggered activity, and potentiation. *Circ Res*, 74(6):1097–1113, Jun 1994.

[73] B. J. Maron and S. E. Epstein. Hypertrophic cardiomyopathy. recent observations regarding the specificity of three hallmarks of the disease: asymmetric septal hypertrophy, septal disorganization and systolic anterior motion of the anterior mitral leaflet. *Am J Cardiol*, 45(1):141–154, Jan 1980.

[74] B. J. Maron, J. K. Wolfson, and W. C. Roberts. Relation between extent of cardiac muscle cell disorganization and left ventricular wall thickness in hypertrophic cardiomyopathy. *Am J Cardiol*, 70(7):785–790, Sep 1992.

[75] R. E. McAllister, D. Noble, and R. W. Tsien. Reconstruction of the electrical activity of cardiac Purkinje fibres. *J Physiol*, 251(1):1–59, Sep 1975.

[76] F. L. Meijler and M. J. Janse. Morphology and electrophysiology of the mammalian atrioventricular node. *Physiol Rev*, 68(2):608–647, Apr 1988.

[77] William R Mills, Niladri Mal, Matthew J Kiedrowski, Ryan Unger, Farhad Forudi, Zoran B Popovic, Marc S Penn, and Kenneth R Laurita. Stem cell therapy enhances electrical viability in myocardial infarction. *J Mol Cell Cardiol*, 42(2):304–314, Feb 2007.

[78] G. K. MOE, W. C. RHEINBOLDT, and J. A. ABILDSKOV. A computer model of atrial fibrillation. *Am Heart J*, 67:200–220, Feb 1964.

[79] M. Morad, editor. *Molecular physiology and pharmacology of cardiac ion channels and transporters*. Dordrecht ; Boston : Kluwer Academic Publishers, 1996.

[80] Stanley Nattel, Ange Maguy, Sabrina Le Bouter, and Yung-Hsin Yeh. Arrhythmogenic ion-channel remodeling in the heart: heart failure, myocardial infarction, and atrial fibrillation. *Physiol Rev*, 87(2):425–456, Apr 2007.

[81] W Nernst. Zur kinetic der in losung befindlichen korper: Theorie der diffusion. *Z Phys Chem*, 2:613–637, 1888.

[82] Hooke. Nigel F. Efficient simulation of action potential propagation in a bidomain. Technical report, 1992.

[83] D. NOBLE. A modification of the Hodgkin–Huxley equations applicable to Purkinje fibre action and pace-maker potentials. *J Physiol*, 160:317–352, Feb 1962.

[84] A. Nygren, C. Fiset, L. Firek, J. W. Clark, D. S. Lindblad, R. B. Clark, and W. R. Giles. Mathematical model of an adult human atrial cell: the role of K+ currents in repolarization. *Circ Res*, 82(1):63–81, 1998.

[85] Christopher S Oehmen, Wayne R Giles, and Semahat S Demir. Mathematical model of the rapidly activating delayed rectifier potassium current I(Kr) in rabbit sinoatrial node. *J Cardiovasc Electrophysiol*, 13(11):1131–1140, Nov 2002.

[86] S. V. Pandit, R. B. Clark, W. R. Giles, and S. S. Demir. A mathematical model of action potential heterogeneity in adult rat left ventricular myocytes. *Biophys J*, 81(6):3029–3051, Dec 2001.

[87] Sandeep V Pandit, Wayne R Giles, and Semahat S Demir. A mathematical model of the electrophysiological alterations in rat ventricular myocytes in type-I diabetes. *Biophys J*, 84(2 Pt 1):832–841, Feb 2003.

[88] Steven Poelzing and David S Rosenbaum. Altered connexin43 expression produces arrhythmia substrate in heart failure. *Am J Physiol Heart Circ Physiol*, 287(4):H1762–H1770, Oct 2004.

[89] L. Priebe and D. J. Beuckelmann. Simulation study of cellular electric properties in heart failure. *Circ Res*, 82(11):1206–1223, Jun 1998.

[90] J. L. Puglisi, R. A. Bassani, J. W. Bassani, J. N. Amin, and D. M. Bers. Temperature and relative contributions of Ca transport systems in cardiac myocyte relaxation. *Am J Physiol*, 270(5 Pt 2):H1772–H1778, May 1996.

[91] J. L. Puglisi and D. M. Bers. LabHEART: an interactive computer model of rabbit ventricular myocyte ion channels and Ca transport. *Am J Physiol Cell Physiol*, 281(6):C2049–C2060, Dec 2001.

[92] Jose L Puglisi, Fei Wang, and Donald M Bers. Modeling the isolated cardiac myocyte. *Prog Biophys Mol Biol*, 85(2-3):163–178, 2004.

[93] M. P. Pye and S. M. Cobbe. Arrhythmogenesis in experimental models of heart failure: the role of increased load. *Cardiovasc Res*, 32(2):248–257, Aug 1996.

[94] Z. Qu and A. Garfinkel. An advanced algorithm for solving partial differential equation in cardiac conduction. *IEEE Trans Biomed Eng*, 46(9):1166–1168, Sep 1999.

[95] W. Quan and Y. Rudy. Unidirectional block and reentry of cardiac excitation: a model study. *Circ Res*, 66(2):367–382, Feb 1990.

[96] R. J. Ramirez, S. Nattel, and M. Courtemanche. Mathematical analysis of canine atrial action potentials: rate, regional factors, and electrical remodeling. *Am J Physiol Heart Circ Physiol*, 279(4):H1767–H1785, Oct 2000.

[97] Roger C. Barr Robert Plonsey. *Bioelectricity: A Quantitative Approach,*. Springer; 2nd edition, 2000.

[98] Wilhelm Roell, Thorsten Lewalter, Philipp Sasse, Yvonne N Tallini, Bum-Rak Choi, Martin Breitbach, Robert Doran, Ulrich M Becher, Seong-Min Hwang, Toktam Bostani, Julia von Maltzahn, Andreas Hofmann, Shaun Reining, Britta Eiberger, Bethann Gabris, Alexander

Pfeifer, Armin Welz, Klaus Willecke, Guy Salama, Jan W Schrickel, Michael I Kotlikoff, and Bernd K Fleischmann. Engraftment of connexin 43-expressing cells prevents post-infarct arrhythmia. *Nature*, 450(7171):819–824, Dec 2007.

[99] S. Rohr, J. P. Kucera, and A. G. Klber. Slow conduction in cardiac tissue, I: effects of a reduction of excitability versus a reduction of electrical coupling on microconduction. *Circ Res*, 83(8):781–794, Oct 1998.

[100] Bradley J. Roth. *Cardiac electrophysiology: From cell to bedside*, chapter Two-dimensional propagation in cardiac muscle, pages 267–272. Philadelphia: Saunders, 2004.

[101] Y. Rudy and W. L. Quan. A model study of the effects of the discrete cellular structure on electrical propagation in cardiac tissue. *Circ Res*, 61(6):815–823, Dec 1987.

[102] Yoram Rudy and Jonathan R Silva. Computational biology in the study of cardiac ion channels and cell electrophysiology. *Q Rev Biophys*, 39(1):57–116, Feb 2006.

[103] S. Rush and H. Larsen. A practical algorithm for solving dynamic membrane equations. *IEEE Trans Biomed Eng*, 25(4):389–392, Jul 1978.

[104] Frank B. Sachse. *Computational cardiology : modeling of anatomy, electrophysiology, and mechanics*, volume 2966. Berlin ; New York : Springer, January 2004.

[105] J. J. Salata, N. K. Jurkiewicz, B. Jow, K. Folander, P. J. Guinosso, B. Raynor, R. Swanson, and B. Fermini. IK of rabbit ventricle is composed of two currents: evidence for IKs. *Am J Physiol*, 271(6 Pt 2):H2477–H2489, Dec 1996.

[106] H. Satoh, L. M. Delbridge, L. A. Blatter, and D. M. Bers. Surface:volume relationship in cardiac myocytes studied with confocal microscopy and membrane capacitance measurements: species-dependence and developmental effects. *Biophys J*, 70(3):1494–1504, Mar 1996.

[107] Nicholas J Severs, Alexandra F Bruce, Emmanuel Dupont, and Stephen Rothery. Remodelling of gap junctions and connexin expression in diseased myocardium. *Cardiovasc Res*, 80(1):9–19, Oct 2008.

[108] R. M. Shaw and Y. Rudy. Ionic mechanisms of propagation in cardiac tissue. Roles of the sodium and L-type calcium currents during reduced excitability and decreased gap junction coupling. *Circ Res*, 81(5):727–741, Nov 1997.

[109] M. S. Spach and P. C. Dolber. Relating extracellular potentials and their derivatives to anisotropic propagation at a microscopic level in human cardiac muscle. evidence for electrical uncoupling of side-to-side fiber connections with increasing age. *Circ Res*, 58(3):356–371, Mar 1986.

[110] M. S. Spach and J. F. Heidlage. The stochastic nature of cardiac propagation at a microscopic level. Electrical description of myocardial architecture and its application to conduction. *Circ Res*, 76(3):366–380, Mar 1995.

[111] M. S. Spach, J. F. Heidlage, P. C. Dolber, and R. C. Barr. Extracellular discontinuities in cardiac muscle: evidence for capillary effects on the action potential foot. *Circ Res*, 83(11):1144–1164, Nov 1998.

[112] M. S. Spach, J. F. Heidlage, P. C. Dolber, and R. C. Barr. Electrophysiological effects of remodeling cardiac gap junctions and cell size: experimental and model studies of normal cardiac growth. *Circ Res*, 86(3):302–311, Feb 2000.

[113] M. S. Spach, J. F. Heidlage, P. C. Dolber, and R. C. Barr. Changes in anisotropic conduction caused by remodeling cell size and the cellular distribution of gap junctions and Na(+) channels. *J Electrocardiol*, 34 Suppl:69–76, 2001.

[114] M. S. Spach, W. T. Miller, P. C. Dolber, J. M. Kootsey, J. R. Sommer, and C. E. Mosher. The functional role of structural complexities in the propagation of depolarization in the atrium of

the dog. cardiac conduction disturbances due to discontinuities of effective axial resistivity. *Circ Res*, 50(2):175–191, Feb 1982.

[115] M. S. Spach, W. T. Miller, D. B. Geselowitz, R. C. Barr, J. M. Kootsey, and E. A. Johnson. The discontinuous nature of propagation in normal canine cardiac muscle. Evidence for recurrent discontinuities of intracellular resistance that affect the membrane currents. *Circ Res*, 48(1):39–54, Jan 1981.

[116] MS Spach, JF Heidlage, and PC Dolber. *Cardiac Electrophysiology. From Cell to Bedside*, chapter The dual nature of anisotropic discontinous conduction in the heart, pages 213–222. W. B. Saunders Company, Philadelphia, 1999.

[117] Mra Stein, Toon A B van Veen, Carol Ann Remme, Mohamed Boulaksil, Maartje Noorman, Leonie van Stuijvenberg, Roel van der Nagel, Connie R Bezzina, Richard N W Hauer, Jacques M T de Bakker, and Harold V M van Rijen. Combined reduction of intercellular coupling and membrane excitability differentially affects transverse and longitudinal cardiac conduction. *Cardiovasc Res*, 83(1):52–60, Jul 2009.

[118] S. P. Thomas, J. P. Kucera, L. Bircher-Lehmann, Y. Rudy, J. E. Saffitz, and A. G. Kleber. Impulse propagation in synthetic strands of neonatal cardiac myocytes with genetically reduced levels of connexin43. *Circ Res*, 92(11):1209–1216, 2003.

[119] Gordon Tomaselli and Dan M. Roden. *Heart physiology and pathophysiology*, chapter Conceptual Basis for Cardiac Arrhythmology, pages 1–31. San Diego, Calif. ; London : Academic Press, 2001.

[120] Amadou Toure and Candido Cabo. Effect of cell geometry on conduction velocity in a subcellular model of myocardium. *IEEE Trans Biomed Eng*, 57(9):2107–2114, Sep 2010.

[121] H. Toyoshima, Y. D. Park, Y. Ishikawa, S. Nagata, Y. Hirata, H. Sakakibara, K. Shimomura, and R. Nakayama. Effect of ventricular hypertrophy on conduction velocity of activation front in the ventricular myocardium. *Am J Cardiol*, 49(8):1938–1945, Jun 1982.

[122] V. Trpanier-Boulay, C. St-Michel, A. Tremblay, and C. Fiset. Gender-based differences in cardiac repolarization in mouse ventricle. *Circ Res*, 89(5):437–444, Aug 2001.

[123] P. C. Ursell, P. I. Gardner, A. Albala, J. J. Fenoglio, and A. L. Wit. Structural and electrophysiological changes in the epicardial border zone of canine myocardial infarcts during infarct healing. *Circ Res*, 56(3):436–451, Mar 1985.

[124] A. M. Varnava, P. M. Elliott, C. Baboonian, F. Davison, M. J. Davies, and W. J. McKenna. Hypertrophic cardiomyopathy: histopathological features of sudden death in cardiac troponin t disease. *Circulation*, 104(12):1380–1384, Sep 2001.

[125] Z. Wang, J. Feng, H. Shi, A. Pond, J. M. Nerbonne, and S. Nattel. Potential molecular basis of different physiological properties of the transient outward K+ current in rabbit and human atrial myocytes. *Circ Res*, 84(5):551–561, Mar 1999.

[126] S. Weidmann. Electrical constants of trabecular muscle from mammalian heart. *J Physiol*, 210(4):1041–1054, Nov 1970.

[127] S.A.Teukolsky W.T. Vetterling W.H. Press, B.P. Flannery. *Numerical Recipes in C. The Art of Scientific Computing*. Cambridge University Press, Cambridge, 1992.

[128] Rob F Wiegerinck, Arie O Verkerk, Charly N Belterman, Toon A B van Veen, Antonius Baartscheer, Tobias Opthof, Ronald Wilders, Jacques M T de Bakker, and Ruben Coronel. Larger cell size in rabbits with heart failure increases myocardial conduction velocity and qrs duration. *Circulation*, 113(6):806–813, Feb 2006.

[129] N. Wiener and A. Rosenbueth. The mathematical formulation of the problem of conduction of impulses in a network of connected excitable elements, specifically in cardiac muscle. *Archos. Del. Instit. De Cardiologia De Mexico*, 16:205–265, 1946.

[130] R. L. Winslow, J. Rice, S. Jafri, E. Marbn, and B. O'Rourke. Mechanisms of altered excitation-contraction coupling in canine tachycardia-induced heart failure, II: model studies. *Circ Res*, 84(5):571–586, Mar 1999.

[131] J. Wu and D. P. Zipes. Effects of spatial segmentation in the continuous model of excitation propagation in cardiac muscle. *J Cardiovasc Electrophysiol*, 10(7):965–972, Jul 1999.

[132] Jiaquan Xu, Kenneth D Kochanek, Sherry L Murphy, and Betzaida Tejada-Vera. Deaths: Final data for 2007. *National Vital Statistic Reports*, 58(19), May 2010.

[133] Lior Yankelson, Yair Feld, Tal Bressler-Stramer, Ilanit Itzhaki, Irit Huber, Amira Gepstein, Doron Aronson, Shimon Marom, and Lior Gepstein. Cell therapy for modification of the myocardial electrophysiological substrate. *Circulation*, 117(6):720–731, Feb 2008.

[134] J. A. Yao, D. E. Gutstein, F. Y. Liu, G. I. Fishman, and A. L. Wit. Cell coupling between ventricular myocyte pairs from connexin43-deficient murine hearts. *Circ Res*, 93(8):736–743, 2003.

[135] Jian-An Yao, Wajid Hussain, Pravina Patel, Nicholas S Peters, Penelope A Boyden, and Andrew L Wit. Remodeling of gap junctional channel function in epicardial border zone of healing canine infarcts. *Circ Res*, 92(4):437–443, Mar 2003.

[136] J. Zeng, K. R. Laurita, D. S. Rosenbaum, and Y. Rudy. Two components of the delayed rectifier K+ current in ventricular myocytes of the guinea pig type. Theoretical formulation and their role in repolarization. *Circ Res*, 77(1):140–152, Jul 1995.

[137] H. Zhang, A. V. Holden, I. Kodama, H. Honjo, M. Lei, T. Varghese, and M. R. Boyett. Mathematical models of action potentials in the periphery and center of the rabbit sinoatrial node. *Am J Physiol Heart Circ Physiol*, 279(1):H397–H421, Jul 2000.

[138] W. X. Zhu, S. B. Johnson, R. Brandt, J. Burnett, and D. L. Packer. Impact of volume loading and load reduction on ventricular refractoriness and conduction properties in canine congestive heart failure. *J. Am. Coll. Cardiol*, 30(3):825–833, 1997.